This is the peer-reviewed, final accepted version for American Mineralogist, published by the Mineralogical Society of America.
The published version is subject to change. Cite as Authors (Year) Title. American Mineralogist, in press.
DOI: https://doi.org/10.2138/am-2022-8014. http://www.minsocam.org/

REVISION 2

Word count: 8357 words

ATOMIC-SCALE STRUCTURE AND NON-STOICHIOMETRY OF METEORITIC HIBONITE: A TRANSMISSION ELECTRON MICROSCOPE STUDY

Jangmi Han[1,2,*], Ichiro Ohnishi[3], Akira Yasuhara[3], Lindsay P. Keller[2]

[1]Lunar and Planetary Institute, USRA, 3600 Bay Area Boulevard, Houston, TX 77058, USA

[2]Astromaterials Research and Exploration Science, NASA Johnson Space Center, 2101 NASA Parkway, Houston, TX 77058, USA

[3]JEOL Ltd., 3-1-2 Musashino, Akishima, Tokyo, 196-8558, Japan

*Corresponding author. Email address: jhan28@Central.UH.EDU. Present address: Department of Earth and Atmospheric Sciences, University of Houston, Houston, TX 77204, USA.

Submitted to *American Mineralogist*, February 12, 2021

Revised, April 19, 2021

ABSTRACT

Hibonite ($CaAl_{12}O_{19}$) is a common refractory mineral in Ca-Al-rich inclusions (CAIs) in primitive meteorites. Transmission electron microscope (TEM) studies have identified enigmatic planar defects in different occurrences of hibonite in the Allende meteorite that give rise to strong streaking along *c** in electron diffraction patterns. Atomic resolution high-angle annular dark-field (HAADF) imaging and energy dispersive X-ray (EDX) analyses were used to

Always consult and cite the final, published document. See http:/www.minsocam.org or GeoscienceWorld

This is the peer-reviewed, final accepted version for American Mineralogist, published by the Mineralogical Society of America.
The published version is subject to change. Cite as Authors (Year) Title. American Mineralogist, in press.
DOI: https://doi.org/10.2138/am-2022-8014. http://www.minsocam.org/

determine the nature and origin of these planar features. HAADF images of hibonite grains reveal lamellar intergrowths of common 1.6 nm spacing, and less commonly 2.0 nm and 2.5 nm spacings, interspersed in stoichiometric hibonite showing 1.1 nm (002) spacing. Stoichiometric hibonite consists of alternating Ca-containing ("R") and spinel-structured ("S") blocks stacked in a sequence RS. In contrast, the 1.6 nm layers result from a doubled S block such that the stacking sequence is RSS, while in the widest defect observed, the stacking sequence is RSSSS. These intergrowths are epitaxial and have coherent, low-strain boundaries with the host hibonite.

Meteoritic hibonite shows common Ti and Mg substitution for Al in its structure. Atomic-resolution EDX maps of hibonite grains in the Allende CAI confirm the preferred site occupancy of Mg on tetragonal M3 sites in S blocks and of Ti on trigonal bipyramidal M2 and octahedral M4 sites in R blocks. Mg is highly concentrated, but Ti is absent, in the planar defects where wider S blocks show Al-rich compositions compared to stoichiometric $MgAl_2O_4$ spinel. Therefore, Mg likely played the major role in the formation and metastability of planar defects in hibonite. Electron energy loss spectroscopy data from the Ti $L_{2,3}$ edge show the presence of mixed Ti oxidation states with ~15-20% of Ti as Ti^{3+} in hibonite, suggesting a direct substitution of $Ti^{3+} \leftrightarrow Al^{3+}$ in hibonite. The remaining ~80-85% of Ti is present as Ti^{4+} and corresponding EDX analyses are consistent with the well-known coupled substitution $2Al^{3+} \leftrightarrow Ti^{4+} + Mg^{2+}$ being the major mechanism for Ti and Mg substitution in hibonite.

The formation of planar defects in hibonite occurred during high-temperature nebular condensation or melting/crystallization processes. The occurrence of non-stoichiometric hibonite in the Allende CAI deviates from the mineral formation sequence predicted from equilibrium condensation models. Overall, our atomic resolution TEM observations signify non-equilibrium, kinetic-controlled crystal growth during high-temperature formation of refractory solids in the

Always consult and cite the final, published document. See http:/www.minsocam.org or GeoscienceWorld

This is the peer-reviewed, final accepted version for American Mineralogist, published by the Mineralogical Society of America.
The published version is subject to change. Cite as Authors (Year) Title. American Mineralogist, in press.
DOI: https://doi.org/10.2138/am-2022-8014. http://www.minsocam.org/

early solar nebula.

Keywords: Hibonite, spinel, calcium-aluminum-rich inclusions, planar defect, transmission electron microscopy

INTRODUCTION

The mineralogy and petrography of primitive carbonaceous chondrite meteorites provide a window into events that occurred at the birth of our Solar System ~4.567 billion years ago (Connelly et al. 2012). A pivotal event in meteorite studies was the fall of the Allende meteorite in 1969 and the recognition of inclusions of high-temperature refractory minerals that formed by gas-solid condensation reactions in the early solar nebula (e.g., Grossman 1972). These refractory inclusions are referred to as Ca-Al-rich inclusions (CAIs) and consist of complex assemblages of minerals such as spinel, melilite (gehlenite ($Ca_2Al_2SiO_7$) - åkermanite ($Ca_2MgSi_2O_7$) solid solution), Al-Ti-rich diopside, perovskite, and other less refractory minerals. The most refractory earliest-formed minerals include corundum and Ca-aluminates such as hibonite ($CaAl_{12}O_{19}$), grossite ($CaAl_4O_7$), and krotite ($CaAl_2O_4$) (Grossman 2010). The Zr- and/or Sc-rich ultrarefractory minerals such as allendeite ($Sc_4Zr_3O_{12}$), panguite ($(Ti,Al,Sc,Mg,Zr,Ca)_{1.8}O_3$), and warkite ($Ca_2Sc_6Al_6O_{20}$) are also present in various CAIs (e.g., Krot et al. 2019; Ma et al. 2020).

Hibonite is of particular interest because it is one of the most important and common primary refractory phases that occurs in many CAIs from different primitive meteorite groups (MacPherson 2014). Hibonite is predicted as one of the earliest phases to condense from a cooling gas of solar composition (e.g., Grossman 2010) and therefore likely records conditions and processes of early and high-temperature events during the Solar System formation. Previous

Always consult and cite the final, published document. See http:/www.minsocam.org or GeoscienceWorld

This is the peer-reviewed, final accepted version for American Mineralogist, published by the Mineralogical Society of America.
The published version is subject to change. Cite as Authors (Year) Title. American Mineralogist, in press.
DOI: https://doi.org/10.2138/am-2022-8014. http://www.minsocam.org/

studies of hibonite crystals and hibonite-bearing CAIs from carbonaceous chondrites have shown that they preserve a diversity of trace element abundance patterns and Ca, Ti, and Mg isotopic compositions that can be directly linked to the chemical and isotopic evolution of the early solar nebula (e.g., Ireland 1988, 1990; Sahijpal et al. 2000; Liu et al. 2009; Davis et al. 2018; Kööp et al. 2018). For example, Liu et al. (2019) found two populations of small fine-grained CAIs in the pristine ALHA77307 CO3.0 chondrite that have well-defined $^{26}Al/^{27}Al$ ratios of 5.4×10^{-5} and 4.9×10^{-5}. The former value is interpreted as the timing for the onset of dust condensation in the protoplanetary disk and the latter value associated with a later thermal isotopic re-equilibration event that affected early-formed CAIs. In addition, the presence of mixed Ti^{3+}-Ti^{4+} oxidation states in hibonite provides a measure of the oxygen fugacities that existed at the time when hibonite formed and was subsequently processed in the early solar nebula (e.g., Ihinger and Stolper 1986; Beckett et al. 1988; Simon et al. 1997, 2001; Giannini et al. 2011; Zega et al. 2012; Doyle et al. 2016).

In addition to chemical and isotopic tracers of nebular processes, the microstructures of refractory minerals in CAIs as revealed by transmission electron microscope (TEM) studies also provide unique insights into the formation and evolution of early formed nebular phases (e.g., Barber et al. 1984; Doukhan et al. 1991; Bolser et al. 2016; Zega et al. 2016; Han and Brearley 2017). Previous TEM observations of CAIs showed two important microstructures of hibonite compared to other common CAI minerals such as spinel and melilite. First, hibonite in CAIs and their rims from carbonaceous chondrites contains abundant planar defects along the (001) plane that are often correlated with Mg enrichments and Ti depletions (Keller 1991; Han et al. 2015, 2017; Needham et al. 2017; Han et al. 2020). The defects were interpreted to have the compositional characteristics of Mg-enriched, non-stoichiometric hibonite, separated by regions

Always consult and cite the final, published document. See http:/www.minsocam.org or GeoscienceWorld

This is the peer-reviewed, final accepted version for American Mineralogist, published by the Mineralogical Society of America.
The published version is subject to change. Cite as Authors (Year) Title. American Mineralogist, in press.
DOI: https://doi.org/10.2138/am-2022-8014. http://www.minsocam.org/

of normal hibonite stoichiometry (Schmid and De Jonghe 1983; Han et al. 2015). Second, hibonite in spinel-rich CAIs from carbonaceous chondrites often shares a consistent crystallographic orientation relationship with adjacent spinel, such that $(001)_{hibonite}//(111)_{spinel}$ (Han et al. 2015, 2017; Needham et al. 2017; Han et al. 2019). This relationship provides strong evidence that the structural similarity between hibonite and spinel enabled epitaxial nucleation and growth of spinel on hibonite surfaces, thereby kinetically inhibiting melilite formation (MacPherson et al. 1984; Beckett and Stolper 1994; Simon et al. 2006; Han et al. 2015). Overall, these observations highlight the notable deviations from the mineral formation sequence predicted from equilibrium condensation calculations, implying that non-equilibrium, kinetically controlled growth modes were important during high-temperature events in the early solar nebula (Toppani et al. 2006; Han et al. 2015).

Recent advances in TEM imaging and microanalysis have enabled sub-angstrom resolution imaging and atomic-scale X-ray analysis (Ohnishi et al. 2018). Here we present the TEM results of atomic resolution imaging and elemental mapping of hibonite in a melilite-rich CAI from the Allende meteorite to better characterize the crystal structure and chemistry of hibonite, as well as spinel that is commonly associated with hibonite in many CAIs from carbonaceous chondrites. Of particular interest for this study is the crystal chemical role of Ti and Mg substitution in the formation of hibonite and comparative TEM analyses of synthetic hibonite. The microstructural features in hibonite provide important constraints on the astrophysical conditions that existed during the formation of refractory solids in the early solar nebula.

SAMPLES

Always consult and cite the final, published document. See http:/www.minsocam.org or GeoscienceWorld

This is the peer-reviewed, final accepted version for American Mineralogist, published by the Mineralogical Society of America.
The published version is subject to change. Cite as Authors (Year) Title. American Mineralogist, in press.
DOI: https://doi.org/10.2138/am-2022-8014. http://www.minsocam.org/

Meteoritic hibonite

The CAI *LK44* is a partial fragment of a large cm-sized compact Type A CAI from the oxidized CV3 carbonaceous chondrite Allende (Fig. 1a). This inclusion is dominated by coarse-grained gehlenitic melilite ($Åk_{\sim 15\text{-}20}$) with fine-grained inclusions of spinel, hibonite, perovskite, paqueite, and grossmanite, which is overlain by an altered Wark-Lovering (WL) rim. Hibonite also occurs as the base layer of the WL rim from this CAI, where Keller (1991) previously reported TEM observations of stacking disorder in hibonite. For this study, we focused on a cluster of spinel and hibonite grains embedded in melilite, in which elongated hibonite grains are partially surrounded by spinel and minor perovskite (Fig. 1b). The electron microprobe measurements show a narrow range of compositions for spinel and hibonite: the spinel is close to end-member $MgAl_2O_4$ with FeO ≤1 wt%, while the hibonite grains contain 3.4-3.7 wt% MgO and 6.7-7.5 wt% TiO_2 (Table 1). However, scanning electron microscope (SEM) X-ray mapping reveals an oscillatory Ti and Mg zonation in hibonite grains (Fig. 1c), and quantitative TEM energy-dispersive X-ray (EDX) analyses show a range in their composition of ~2-8 wt% TiO_2 and ~1-5 wt% MgO.

Synthetic hibonite

Synthetic hibonite was prepared following the procedures in Schmid and DeJonghe (1983) by reacting pure alumina crucibles with a $2CaO\text{-}Al_2O_3$ composition eutectic melt ± 5 wt% MgO ± $CaTiO_3$ in air for 4 hours or 5 days at 1530°C, followed by air quenching. The run products were cross-sectioned, mounted in epoxy, and polished for detailed petrologic and mineralogical descriptions, as well as for TEM section preparation. In all experiments, the reaction zone adjacent to alumina shows a similar mineral sequence from hibonite, grossite, to krotite with a

Always consult and cite the final, published document. See http:/www.minsocam.org or GeoscienceWorld

This is the peer-reviewed, final accepted version for American Mineralogist, published by the Mineralogical Society of America.
The published version is subject to change. Cite as Authors (Year) Title. American Mineralogist, in press.
DOI: https://doi.org/10.2138/am-2022-8014. http://www.minsocam.org/

quenched melt glass. Experiments where MgO was added also produced spinel laths intergrown with hibonite in experiment (2) and euhedral spinel grains in the quenched melt in experiments (2-4). A summary of the experimental conditions and results for the five experiments is given in Table 2, and representative SEM back-scattered electron (BSE) images of the reaction zones are shown in Figure 2.

ANALYTICAL METHODS

For a detailed TEM analysis, two sections, FIB-A and FIB-B, were prepared from a single hibonite crystal in the CAI *LK44* (Fig. 1b), using a FEI Quanta 3D 600 dual beam focused ion beam (FIB)/SEM at NASA Johnson Space Center (JSC). Additional FIB sections were prepared from hibonite crystals in the reaction zone of the five run products using the same FIB/SEM instrument. All the FIB sections were cut normal to the elongation direction of the hibonite crystals.

Initial structural and chemical characterization of all FIB sections from both meteoritic and synthetic hibonites was performed using a JEOL 2500SE 200 kV field-emission scanning TEM (STEM) at NASA JSC. Bright-field (BF) STEM and high-resolution (HR) TEM images and selected area electron diffraction patterns were collected. Elemental mapping and quantitative microanalyses were carried out using a Thermo-Noran thin-window EDX spectrometer. Elemental X-ray maps were obtained using STEM raster mode with a scanned probe size of 2 nm and a dwell time of 50 μs/pixel. Successive rasters were added until <1% counting statistical errors were achieved for major elements. Data reduction was performed using the Cliff-Lorimer thin film approximation with experimental and theoretical K-factors determined from natural and synthetic standards.

Always consult and cite the final, published document. See http:/www.minsocam.org or GeoscienceWorld

This is the peer-reviewed, final accepted version for American Mineralogist, published by the Mineralogical Society of America.
The published version is subject to change. Cite as Authors (Year) Title. American Mineralogist, in press.
DOI: https://doi.org/10.2138/am-2022-8014. http://www.minsocam.org/

For atomic resolution high-angle annular dark-field (HAADF) imaging and elemental X-ray mapping, two TEMs were utilized at JEOL in Japan. In the first session, FIB-A was analyzed using a JEOL JEM-F200 STEM. This instrument is a 200 kV cold field emission gun STEM, equipped with HAADF detector, dual 100 mm^2 silicon drift detectors, and a Gatan imaging filter for electron energy loss spectroscopy (EELS). Regions of interest were mapped using a probe of 150 pA current and 0.1 nm size, with a dwell time of 20 μs/pixel. Successive image frames were added until acceptable counting statistics were achieved (typically <5 minutes). In the following session, FIB-B was analyzed using a JEOL JEM-ARM300F GrandARM STEM. This instrument is an aberration-corrected electron microscope, equipped with a cold field emission gun, HAADF detector, dual 158 mm^2 silicon drift detectors, and a Gatan imaging filter for EELS. Regions of interest were mapped using a probe of 85 pA current and ~80 pm size, with a dwell time of 10 μs/pixel, by operating at 200 kV accelerate voltage. Successive image frames were added until acceptable counting statistics were achieved (typically <2 minutes). All hibonite crystals in both FIB sections were tilted into the [$1\bar{1}0$] zone for the record of imaging and X-ray mapping.

RESULTS AND DISCUSSION

Planar defects in hibonite

In low magnification BF STEM images, hibonite grains in the CAI *LK44* exhibit planar defects normal to the *c* axis, in contrast to coexisting spinel, melilite, and perovskite that are featureless and defect-free (Fig. 3). Most defects are developed along the full length of the hibonite grains, but a few show terminations within the grains. The defect density varies among and within the hibonite grains. In FIB-A, only one hibonite grain (HIB-1; Figs. 3a-c) contains a high density of defects along one edge that results in strong streaking along the *c* axis in electron

Always consult and cite the final, published document. See http:/www.minsocam.org or GeoscienceWorld

This is the peer-reviewed, final accepted version for American Mineralogist, published by the Mineralogical Society of America.
The published version is subject to change. Cite as Authors (Year) Title. American Mineralogist, in press.
DOI: https://doi.org/10.2138/am-2022-8014. http://www.minsocam.org/

185 diffraction patterns. In FIB-B, a much lower density of defects is observed along the edge of one
186 hibonite grain (HIB-2; Figs. 3d-f), with very weak streaking along the *c* axis in electron
187 diffraction patterns. Similar TEM observations were made from hibonite in different
188 carbonaceous chondrites (Han et al. 2015, 2017; Needham et al. 2017; Han et al. 2020),
189 suggesting the common occurrence of planar defects in meteoritic hibonite.

190 An unusual observation in another hibonite grain in FIB-B (HIB-3; Figs. 3d-e) is the
191 occurrence of defects that are associated with a distinct spinel inclusion (Fig. 4a). The spinel
192 inclusion is anomalously Al-rich with a composition of $Mg_{0.5}Al_{2.3}O_4$ and contains minor V_2O_3
193 (<1 wt%), based on TEM EDX analyses, and should be accompanied by cation vacancies. While
194 exceedingly rare, Al_2O_3 excesses up to ~10 mol% of the $Al_{8/3}O_4$ component in spinel are
195 reported from a few CAIs in carbonaceous chondrites (El Goresy et al. 1984; Simon et al. 1994;
196 Kööp et al. 2016). In general, spinel intergrown with hibonite in least altered CAIs from
197 carbonaceous chondrites is close to pure stoichiometric $MgAl_2O_4$ (e.g., Han et al. 2015, 2019). In
198 addition, fast Fourier transform (FFT) analyses of HRTEM images show a crystallographic
199 orientation relationship between host hibonite and spinel inclusion, such that
200 $[100]_{hibonite}//[011]_{spinel}$ and $(001)_{hibonite}//(111)_{spinel}$ (Figs. 4b-d). Similar relationships were
201 observed from spinel-rich CAIs from carbonaceous chondrites (Han et al. 2015, 2017; Needham
202 et al. 2017; Han et al. 2019).
203

204 **Comparison with synthetic hibonite**

205 The experimental charges all show a typical texture of a layer of hibonite laths with their
206 *c* axis oriented perpendicular to the layer. The hibonite laths from the five run products display a
207 range of planar defect densities and correlated compositional variations. In experiments (1) and

Always consult and cite the final, published document. See http:/www.minsocam.org or GeoscienceWorld

This is the peer-reviewed, final accepted version for American Mineralogist, published by the Mineralogical Society of America.
The published version is subject to change. Cite as Authors (Year) Title. American Mineralogist, in press.
DOI: https://doi.org/10.2138/am-2022-8014. http://www.minsocam.org/

(5), Mg-Ti-free and Ti-bearing hibonite grains are free of defects. In contrast, experiments (2-3) both produced Mg-bearing hibonite grains that commonly contain a high, but similar density of defects normal to the *c* axis (Figs. 5a-b). In experiment (4), some Ti-Mg-bearing hibonite grains contain a low density of defects (Fig. 5c), similar to the defect density observed from hibonite crystals in the CAI *LK44*. The critical observation from our TEM EDX analyses of hibonite from the three experiments (2-4) is that the defects, which appear as the vertical dark band in the BF STEM image, are clearly linked to higher MgO contents, but are not correlated with TiO_2 contents (Fig. 6). We propose that the MgO enrichments along planar defects in Mg-bearing hibonite stabilized the formation of Mg-enriched, non-stoichiometric hibonite, resulting in complex, disordered intergrowths within stoichiometric hibonite. From our limited experiments, we observed no correlation between the defect formation and density with the presence of minor TiO_2 contents in Mg-Ti-bearing hibonite. These results suggest no effects of Ti on the formation of planar defects and correlated non-stoichiometry in hibonite.

Spinel stabilized by the addition of MgO in experiments (2-4) also shows notable textural and compositional variations. Two compositionally distinct spinel occurrences are observed in experiment (2), including: (1) lath-shaped, Al-rich spinel containing 2.14-2.20 Al cations per 4 oxygen anions, intergrown with hibonite, and (2) euhedral, stoichiometric $MgAl_2O_4$ spinel crystals in grossite and in a layer of krotite + quenched glass (Fig. 2a). The Al-rich spinel laths are crystallographically oriented to intergrown hibonite with $(001)_{hibonite}//(111)_{spinel}$, a similar relationship observed from the spinel inclusion in hibonite from the CAI *LK44* (Fig. 4). In contrast, in experiments (3-4), only euhedral, stoichiometric $MgAl_2O_4$ spinel crystals occur as inclusions in grossite and in krotite + quenched glass layer (Figs. 2b-c). The observed significant Al_2O_3 excess in spinel intergrown with hibonite is due to the saturation of a melt with respect to

Always consult and cite the final, published document. See http:/www.minsocam.org or GeoscienceWorld

This is the peer-reviewed, final accepted version for American Mineralogist, published by the Mineralogical Society of America.
The published version is subject to change. Cite as Authors (Year) Title. American Mineralogist, in press.
DOI: https://doi.org/10.2138/am-2022-8014. http://www.minsocam.org/

corundum (Beckett and Stolper 1994; Simon et al. 1994), consistent with a thermodynamic mixing model that predicts up to ~30 mol% of the $Al_{8/3}O_4$ component in spinel at ~1750 K (Navrotsky et al. 1986; Sack 2014). However, the disappearance of Al-rich spinel laths intergrown with hibonite in experiments (3-4) indicates that Al-rich spinel formed metastably owing to very high-temperature, short-lived heating followed by rapid cooling.

Crystal structure and chemistry of hibonite

A crystal structure model of hibonite with an ideal formula $CaAl_{12}O_{19}$ refined by recent single-crystal X-ray diffraction studies (Hofmeister et al. 2004; Nagashima et al. 2010; Giannini et al. 2014) was used to interpret the crystal structure and chemistry of hibonite in the CAI *LK44* as observed by TEM. Hibonite has a hexagonal structure (space group $P6_3/mmc$), in which Ca^{2+} ions occur in 12-fold coordination and Al^{3+} ions are distributed over five interstitial sites, including three octahedral M1, M4, and M5, one tetragonal M3, and one trigonal bipyramidal M2 sites. A chemical formula of hibonite is summarized as $^{[12]}Ca^{[6]}M1^{[5]}M2^{[4]}M3_2{}^{[6]}M4_2{}^{[6]}M5_6O_{19}$, where coordination numbers are given as bracketed superscripts and the multiplicity of the sites is subscripted. Hibonite from carbonaceous chondrites is compositionally complex and contains significant concentrations of other elements, commonly Si^{4+}, $Ti^{3+,4+}$, Fe^{2+}, and Mg^{2+} (Brearley and Jones 1998), all substituting for Al^{3+} on the five M1 to M5 sites (Doyle et al. 2014).

The basic structure of hibonite consists of two different building blocks, labeled "S" and "R", respectively, which alternate normal to the *c* axis (Schmid and De Jonghe 1983; Nagashima et al. 2010). The S block has the ideal composition of $(Al_6O_8)^{2+}$ representing a spinel or γ-alumina structure composed of two cubic close-packed oxygen layers with two octahedral M1

Always consult and cite the final, published document. See http:/www.minsocam.org or GeoscienceWorld

This is the peer-reviewed, final accepted version for American Mineralogist, published by the Mineralogical Society of America.
The published version is subject to change. Cite as Authors (Year) Title. American Mineralogist, in press.
DOI: https://doi.org/10.2138/am-2022-8014. http://www.minsocam.org/

and M5 and one tetragonal M3 sites. The R block with a composition of $(CaAl_6O_{11})^{2-}$ represents an intermediate mirror plane composed of three hexagonal close-packed oxygen layers comprising Ca with one trigonal bipyramidal M2 and one octahedral M4 sites. A unit cell of hibonite is characterized by a stacking sequence of RSR*S* parallel to the (001) plane, where R* and S* are structurally same as R and S but rotated by 180° with respect to R and S around the *c* axis. This neutral RS subunit is therefore the primitive repeating unit of hibonite structure with a total composition of $CaAl_{12}O_{19}$, corresponding to the (002) lattice fringe spacing of 1.1 nm normal to the *c* axis observed in HRTEM images. Schmid and De Jonghe (1983) observed different spacings of the (001) and (002) reflections in HRTEM images of synthetic hibonite, which were interpreted as syntactic intergrowths by altering the stacking sequence of R and S blocks in the hibonite structure, similar to that observed in manetoplumbite-related structures (e.g., Hirotsu and Sato 1978; Göbbels et al. 1995; Iyi et al. 1995).

Our atomic resolution HAADF images reveal variations in (00*l*) fringe spacings along *c** in hibonite crystals from the CAI *LK44* (Figs. 7-8). The *d*-spacings of the (002) fringes in the HAADF images were measured between successive brightest fringes arising from Ca atoms. In HIB-1 and HIB-2, isolated 1.6 nm layers are common and randomly distributed within the normal 1.1 nm layers of stoichiometric hibonite (Figs. 7a-c). We also observed a single layer of 2.5 nm spacing in HIB-2 (Figs. 7c-d). In HIB-3, an Al-rich spinel inclusion is decorated by a single 1.6 nm layer along its top (Fig. 8a), as well as stepwise 2.0 nm layers extended from its bottom end (Figs. 8b-d), which may have grown along the *c* axis screw dislocation in hibonite. Collectively, single 1.6 nm layers mixed in various proportions inside the regular hibonite structure of 1.1 nm (002) spacing are the most common, but less-common wider layers of 2.0 nm and 2.5 nm (002) spacings also occur as noted above. These layers and the Al-rich spinel

Always consult and cite the final, published document. See http:/www.minsocam.org or GeoscienceWorld

This is the peer-reviewed, final accepted version for American Mineralogist, published by the Mineralogical Society of America.
The published version is subject to change. Cite as Authors (Year) Title. American Mineralogist, in press.
DOI: https://doi.org/10.2138/am-2022-8014. http://www.minsocam.org/

277 inclusion share low strain grain boundaries with the host hibonite crystals.

278 The observed spacing variations in hibonite crystals from the CAI *LK44* are interpreted
279 directly as different stacking ratios of two basic R and S blocks, without changing the basic
280 structural characteristics of these blocks. That is, as shown by Schmid and De Jonghe (1983),
281 such variations are explained as unit cell scale syntactic intergrowths in terms of the structural
282 block concept and are distinguished from common stacking faults that involve shear. We used
283 the Crystal Marker^{TM} software and the structure determination from Nagashima et al. (2010) to
284 project the crystal structure in terms of the arrangement of R and S blocks on our HADDF
285 images (Fig. 9). As discussed above, prominent lattice fringes of 1.1 nm represent a perfectly
286 ordered, stoichiometric hibonite crystal consisting of a coherent growth of repeating RS units.
287 The common 1.6 nm wide (002) layers are composed of a stacking sequence of a RSS unit that
288 accommodates six, instead of four, oxygen planes (Fig. 9a). These defect layers contain twice as
289 many octahedral M1 and tetragonal M3 sites and 50% more octahedral M5 sites, compared to
290 stoichiometric hibonite, and have an idealized stoichiometry of
291 $^{[12]}Ca^{[6]}M1_2{}^{[5]}M2^{[4]}M3_4{}^{[6]}M4_2{}^{[6]}M5_9O_{28}$ with a total composition of $CaAl_{18}O_{28}$. The 2.0 nm and
292 2.5 nm wide (002) layers both lack bright fringes of Ca, but contain distinct lamellae composed
293 of 0.46 nm (002) spacing corresponding to the (111) spacing of a cubic spinel or γ-alumina
294 structure (Figs. 8d, 9b). We conclude that the 2.0 nm and 2.5 nm layers are stacked in a sequence
295 of RSSS and RSSSS, respectively, which represent metastable spinel lamellae that are epitaxially
296 intergrown with stoichiometric hibonite on the unit cell scale. Collectively, the observed wider
297 spacings in hibonite are due to its distinct structural ability to accommodate coherent (001)
298 intergrowths of additional S blocks into the RS sequence of stoichiometric hibonite. The inferred
299 systematic structural variation in hibonite is evidence for non-stoichiometry, and our atomic

Always consult and cite the final, published document. See http:/www.minsocam.org or GeoscienceWorld

This is the peer-reviewed, final accepted version for American Mineralogist, published by the Mineralogical Society of America.
The published version is subject to change. Cite as Authors (Year) Title. American Mineralogist, in press.
DOI: https://doi.org/10.2138/am-2022-8014. http://www.minsocam.org/

300 resolution X-ray mapping shows a prominent Mg increase, but Ca and Ti deficiencies in the 1.6
301 nm and 2.5 nm layers (Fig. 10), due to the preferred site occupancy of Mg on tetragonal M3 sites
302 in S blocks (Nagashima et al. 2010; Doyle et al. 2014; Giannini et al. 2014; this study).
303 Interestingly, we did not observe any layers with a sequence of RRS or isolated R blocks,
304 suggesting that S blocks are necessary for the stability of hibonite structure containing
305 intergrowth phases (Schmid and De Jonghe 1983; Göbbels et al. 1995; Iyi et al. 1995).

306 Our atomic resolution HAADF imaging results can also be interpreted within the
307 framework of polysomatic series (Thompson 1978; Veblen 1991), since hibonite has a layered
308 structure consisting of alternating R and S blocks parallel to the (001) plane (Hofmeister et al.
309 2004; Nagashima et al. 2010). In this view, hibonite is a polysomatic mineral that can contain
310 different stacking ratios of two structurally and chemically distinct R and S modules, leading to
311 variations in structures and stoichiometries. The observed layers of 1.6 nm, 2.0 nm, and 2.5 nm
312 spacings in hibonite having 1.1 nm (002) spacing (Figs. 7-8) are thus regarded as a polysomatic
313 series of intergrowth structures, in which the number of S modules stacked with one R module is
314 systemically varied up to four (Fig. 9), with increased Mg concentrations (Fig. 10).
315

316 **Ti and Mg substitution in hibonite**

317 Atomic resolution HAADF imaging and corresponding atomic-scale X-ray mapping of
318 hibonite from the CAI *LK44* provide direct information about the spatial distribution of atoms in
319 the hibonite structure. As seen in Figure 10, Ti is concentrated along the same plane as the Ca
320 atoms, suggesting its most probable distribution in trigonal bipyramidal M2 and octahedral M4
321 sites. Mg is concentrated between the Ca atom planes, suggesting its most stable occupancy on
322 tetragonal M3 sites. Importantly, Mg concentrations are significantly increased in a layer of 1.6

Always consult and cite the final, published document. See http:/www.minsocam.org or GeoscienceWorld

323 nm (002) spacing, where double tetragonal M3 sites and 50% more octahedral M5 sites are
324 required, compared to those in stoichiometric hibonite, as discussed above. Mg is also
325 concentrated in a wider layer of 2.5 nm (002) spacing, where extra Al-rich spinel occurs
326 epitaxially intergrown with stoichiometric hibonite. Interpretation of the Ti and Mg site
327 distributions from the atomic resolution X-ray mapping is broadly consistent with the site
328 occupancies of Ti and Mg determined from single crystal X-ray diffraction data (Bermane et al.
329 1996; Nagashima et al. 2010; Giannini et al. 2014; Berry et al. 2017) and neutron powder
330 diffraction data combined with density functional theory modeling (Doyle et al. 2014).

331 An important question pertains to the Ti and Mg substitution mechanism(s) in hibonite.
332 Figure 11 summarizes the chemical compositions of hibonite grains from the CAI *LK44*.
333 Hibonite grains exhibit a range of ~2-8 wt% TiO_2 and ~1-5 wt% MgO, with ~1-3 wt% SiO_2, ≤1
334 wt% V_2O_3, and ≤0.6 wt% FeO. These TiO_2 and MgO ranges correspond to almost the entire
335 range previously reported from hibonite in carbonaceous chondrites (Brearley and Jones 1998).
336 With total Ti calculated as Ti^{4+}, there is a good correlation between (Mg + Fe + Ti + Si) vs. (Al +
337 V) cations (Fig. 11a), consistent with the substitutional relationships between cations in hibonite.
338 Many analyses fall close to a 1:1 correlation line on a plot of (Mg + Fe) vs. (Ti + Si) cations (Fig.
339 11b), suggesting that Mg^{2+} is charge balanced with Ti^{4+} and Si^{4+}. Variable amounts of Si, Ti, and
340 Mg are therefore incorporated into hibonite by the coupled substitutions $2Al^{3+} \leftrightarrow Ti^{4+} + Mg^{2+}$
341 and $2Al^{3+} \leftrightarrow Si^{4+} + Mg^{2+}$, with the first being the major mechanism for Ti and Mg incorporations
342 into hibonite. Minor Fe^{2+} present in hibonite is interpreted as secondary substitution for Mg^{2+} in
343 the parent body setting (Simon et al. 2001, 2006). However, some fraction of the analyses plots
344 off the 1:1 line to the Ti-Si-rich side, suggesting the presence of Ti^{3+} that can substitute directly
345 with Al^{3+} and therefore is not coupled with Mg^{2+}. These compositional trends are consistent with

Always consult and cite the final, published document. See http:/www.minsocam.org or GeoscienceWorld

a general characteristic revealed by electron microprobe analyses of hibonite from carbonaceous chondrites (Brearley and Jones 1998).

We used EELS to evaluate the Ti oxidation states in hibonite and perovskite in FIB-A from the CAI *LK44*. The Ti L_3 edge in oxides and silicates consists of two distinct peaks that arise from well-known crystal-field effects and whose positions are sensitive to oxidation states, with Ti^{3+} peaks occurring at energies ~1 eV below corresponding peaks for Ti^{4+} (e.g., Christoffersen et al. 1996; Stoyanov et al. 2007). The EELS data for the Ti $L_{2,3}$ edge in hibonite from the CAI *LK44* show distinct low energy shoulders on the L_3 doublet, which are contributed by Ti^{3+}, whereas perovskite adjacent to hibonite shows only the presence of Ti^{4+} (Fig. 12a). We deconvolved the EELS spectra from the L_3 edge by fitting the peaks with Gaussian profile models and determining the peak area ratios (Fig. 12b). The peak area ratios suggest that ~15-20% of Ti is present as Ti^{3+} in the hibonite, which is within the $Ti^{3+}/\Sigma Ti$ range (~5-35%) reported for hibonite from carbonaceous chondrites (Beckett et al. 1988; Simon et al. 1997; Giannini et al. 2011; Zega et al. 2012; Doyle et al. 2016).

The observed variation in Ti^{3+} amount in hibonite was interpreted as a range of oxygen fugacity ($\log fO2 \approx -16$ to -5) recorded both in the nebular and parent body settings (Ihinger and Stolper 1986; Beckett et al. 1988; Giannini et al. 2011; Zega et al. 2012). That is, hibonite originally formed in a region of solar nebula under highly reducing conditions (Beckett et al. 1998), as inferred from Ti^{3+}/Ti^{4+} ratios in Al-Ti-rich pyroxene in compact Type A and Type B CAIs from Allende (Grossman et al. 2008). Later, it was oxidized *in situ* during thermal processing on the parent body to varying degrees (Ihinger and Stolper 1986; Simon et al. 1997; Zega et al. 2012). However, the application of hibonite chemistry as an oxygen barometer for the early Solar System processes appears questionable because the amount of Ti^{3+} incorporated into

Always consult and cite the final, published document. See http:/www.minsocam.org or GeoscienceWorld

This is the peer-reviewed, final accepted version for American Mineralogist, published by the Mineralogical Society of America.
The published version is subject to change. Cite as Authors (Year) Title. American Mineralogist, in press.
DOI: https://doi.org/10.2138/am-2022-8014. http://www.minsocam.org/

the hibonite structure has been shown experimentally to be largely independent of oxygen fugacities of a gas in equilibrium with hibonite, and instead is strongly controlled by crystal chemistry, especially Mg availability (Doyle et al. 2014, 2016; Berry et al. 2017). Likewise, some of our electron microprobe and TEM EDX analyses show a good correlation between Ti^{4+} and Mg^{2+} cation numbers in hibonite (Table 1; Fig. 11b), indicating that no or minimal direct substitution $Ti^{3+} \leftrightarrow Al^{3+}$ occurred in some hibonite. These observations suggest that Ti^{3+}-bearing and Ti^{3+}-free hibonites can occur within single CAIs, implying their complex redox history in the nebular and/or asteroidal settings.

IMPLICATIONS AND CONCLUSIONS

Our atomic resolution HAADF imaging and X-ray mapping of hibonite from the Allende CAI *LK44* reveal the presence of mixed spacings along the (001) plane and correlated Mg enrichments. This correlation is fully consistent with annealing experiments that showed that the formation of planar defects in hibonite crystals is promoted by the presence of minor Mg. Thus, our TEM analyses of meteoritic and synthetic hibonites clearly demonstrate a strong chemical control on the alteration of stacking sequences of basic S and R blocks in the hibonite structure. The substitution of Mg with Al in tetrahedral M3 sites stabilizes the formation of wider S blocks, hence forming complex, disordered intergrowths of stoichiometric and Mg-enriched, non-stoichiometric hibonites. However, the Ti-Al substitution in trigonal bipyramidal M2 and octahedral M4 sites does not enhance the formation of wider R blocks in hibonite but may require the charge balanced substitution with Mg ($Ti^{4+} + Mg^{2+} \leftrightarrow 2Al^{3+}$). The unit cell scale intergrowths of stoichiometric and non-stoichiometric hibonites indicates that structures with different stacking sequences but similar symmetry have similar free energies and hence co-exist

Always consult and cite the final, published document. See http:/www.minsocam.org or GeoscienceWorld

This is the peer-reviewed, final accepted version for American Mineralogist, published by the Mineralogical Society of America.
The published version is subject to change. Cite as Authors (Year) Title. American Mineralogist, in press.
DOI: https://doi.org/10.2138/am-2022-8014. http://www.minsocam.org/

as kinetically metastable phases on the unit cell scale (Hirotsu and Sato 1978).

The atomic-scale TEM observations of hibonite from the Allende CAI *LK44* provide new insights into formation conditions of refractory solids in the early solar nebula. The non-stoichiometric hibonite and Al-rich spinel inclusion observed in this study suggest that these phases formed metastably but were kinetically stable at very high-temperatures. The Al-rich spinel (up to ~50 mol% of the $Al_{8/3}O_4$ component) formed contemporaneously with hibonite at temperatures <1800 K (Navrotsky et al. 1986; Sack 2014). However, the occurrence of non-stoichiometric, Al-rich spinel conflicts with equilibrium condensation calculations, where a thermodynamic model for $MgAl_2O_4$ - $Al_{8/3}O_4$ spinels (Sack 2014) was used, showing essentially no stability field for this phase, predicting instead an assemblage of stoichiometric corundum, grossite, and krotite, even in highly dust-enriched systems (Ebel et al. 2014). Our observations suggest that the metastable assemblage of hibonite and Al-rich spinel formed in place of thermodynamic equilibrium Ca-Al-oxide assemblages. We thus conclude that non-equilibrium crystal growth was strongly controlled by kinetic factors, such as crystal structure and chemistry and cooling rates, during very high-temperature formation of refractory solids in the early solar nebula (Toppani et al. 2006; Han et al. 2015).

ACKNOWLEDGEMENTS

This study was supported in part by NASA grant 17-EW17-2-0088 (PI: LPK). Part of this work was presented at the Mineralogical Society of America/Geological Society of America special session honoring Peter R. Buseck upon his receiving the MSA Roebling Medal. We thank JEOL Ltd. Japan for access to the F200 and GrandARM TEMs to perform these measurements. The SEM, FIB, and EMPA analyses, and some of the TEM work were done in

Always consult and cite the final, published document. See http:/www.minsocam.org or GeoscienceWorld

This is the peer-reviewed, final accepted version for American Mineralogist, published by the Mineralogical Society of America.
The published version is subject to change. Cite as Authors (Year) Title. American Mineralogist, in press.
DOI: https://doi.org/10.2138/am-2022-8014. http://www.minsocam.org/

415 the Electron Beam Analysis Labs at NASA Johnson Space Center. We thank Emily L. Keller for
416 assistance with the curve fitting and deconvolution of the EELS spectra. We appreciate Dr. Steve
417 Simon and Dr. Chi Ma for their helpful and constructive comments. LPI contribution No. xxxx.
418 LPI is operated by USRA under a cooperative agreement with the Science Mission Directorate of
419 the National Aeronautics and Space Administration.

Always consult and cite the final, published document. See http:/www.minsocam.org or GeoscienceWorld

This is the peer-reviewed, final accepted version for American Mineralogist, published by the Mineralogical Society of America.
The published version is subject to change. Cite as Authors (Year) Title. American Mineralogist, in press.
DOI: https://doi.org/10.2138/am-2022-8014. http://www.minsocam.org/

REFERENCES CITED

Barber, D.J., Martin, P.M., and Hutcheon, I.D. (1984) The microstructure of minerals in coarse-grained Ca–Al-rich inclusions from the Allende meteorite. Geochimica et Cosmochimica Acta, 48, 769–783.

Beckett, J.R., and Stolper, E. (1994) The stability of hibonite, melilite and other aluminous phases in silicate melts: Implications for the origin of hibonite-bearing inclusions from carbonaceous chondrites. Meteoritics, 29, 41–65.

Beckett, J.R., Live, D., Tsay, F.-D., Grossman, L., and Stolper, E. (1988) Ti^{3+} in meteoritic and synthetic hibonite. Geochimica et Cosmochimica Acta, 52, 1479–1495.

Bermanec, V.V., Holtstam, D., Sturman, D., Criddle, A.J., Back, M.E., and Scavnicar, S. (1996) Nezilovite, a new member of the magnetoplumbite group, and the crystal chemistry of magnetoplumbite and hibonite. The Canadian Mineralogist, 34, 1287–1297.

Berry, A.J., Schofield, P.F., Kravtsova, A.N., Miller, L.A., Stephen, N.R., Walker, A.M., Soldatov, A.V., Ireland, T.R., Geraki, K., and Mosselmans, J.F.W. (2017) The limitations of hibonite as a single-mineral oxybarometer for early solar system processes. Chemical Geology, 466, 32–40.

Bolser, D., Zega, T.J., Asaduzzaman, A., Bringuier, S., Simon, S.B., Grossman, L., Thompson, M.S., and Domanik, K.J. (2016) Microstructural analysis of Wark-Lovering rims in the Allende and Axtell CV3 chondrites: implications for high-temperature nebular processes. Meteoritics and Planetary Science, 51, 743–756.

Brearley, A.J., and Jones, R.H. (1998) Chondritic meteorites. In J.J. Papike, Ed., Planetary Materials, 36, p. 3-001–3-398. Reviews in Mineralogy and Geochemistry, Mineralogical Society of America, Chantilly, Virginia.

Always consult and cite the final, published document. See http:/www.minsocam.org or GeoscienceWorld

This is the peer-reviewed, final accepted version for American Mineralogist, published by the Mineralogical Society of America.
The published version is subject to change. Cite as Authors (Year) Title. American Mineralogist, in press.
DOI: https://doi.org/10.2138/am-2022-8014. http://www.minsocam.org/

443 Christoffersen, R., Keller, L.P., and McKay, D.S. (1996) Microstructure, chemistry, and origin of
444 grain rims on ilmenite from the lunar soil finest fraction. Meteoritics and Planetary Science,
445 31, 835–848.

446 Connelly, J.N., Bizzarro, M., Krot, A.N., Nordlund, Å., Wielandt, D., and Ivanova, M.A. (2012)
447 The absolute chronology and thermal processing of solids in the solar protoplanetary disk.
448 Science, 338, 651–655.

449 Davis, A.M., Zhang, J., Greber, N.D., Hu, J., Tissot, F.L.H., and Dauphas, N. (2018) Titanium
450 isotopes and rare earth patterns in CAIs: Evidence for thermal processing and gas-dust
451 decoupling in the protoplanetary disk. Geochimica et Cosmochimica Acta, 221, 275–295.

452 Doukhan, N., Doukhan, J.C., and Poirier, J.P. (1991) Transmission electron microscopy of a
453 refractory inclusion from the Allende meteorite: anatomy of a pyroxene. Meteoritics, 26,
454 105–109.

455 Doyle, P.M., Schofield, P.F., Berry, A.J., Walker, A.M., and Knight, K.S. (2014) Substitution of
456 Ti^{3+} and Ti^{4+} in hibonite ($CaAl_{12}O_{19}$). American Mineralogist, 99, 1369–1382.

457 Doyle, P.M., Berry, A.J., Schofield, P.F., and Mosselmans, J.F.W. (2016) The effect of site
458 geometry, Ti content and Ti oxidation state on the Ti K-edge XANES spectrum of
459 synthetic hibonite. Geochimica et Cosmochimica Acta, 187, 294–310.

460 Ebel, D.S. (2006) Condensation of rocky material in astrophysical environments. In D.S.
461 Lauretta and H.Y. McSween, Eds., Meteorites and the Early Solar System II, p. 253–277.
462 University of Arizona Press, Tucson.

463 Ebel, D.S., Crapster-Pregont, E.J., and Sack, R.O. (2014) Predicted non-stability of Al-rich
464 spinel in the early solar system. Meteoritics and Planetary Science, 49, A101.

465 El Goresy, A., Palme, H., Yabuki, H., Nagel, K., Herrwerth, I., and Ramdohr, P. (1984) A

Always consult and cite the final, published document. See http:/www.minsocam.org or GeoscienceWorld

This is the peer-reviewed, final accepted version for American Mineralogist, published by the Mineralogical Society of America.
The published version is subject to change. Cite as Authors (Year) Title. American Mineralogist, in press.
DOI: https://doi.org/10.2138/am-2022-8014. http://www.minsocam.org/

466 calcium-aluminum-rich inclusion from the Essebi (CM2) chondrite: Evidence for
467 captured spinel-hibonite spherules and for an ultra-refractory rimming sequence.
468 Geochimica et Cosmochimica Acta, 48, 2283–2298.
469 Giannini, M., Ballaran, T.B., Langenhorst, F., and Bischoff, A. (2011) TEM-EELS study of
470 titanium oxidation state in meteoritic hibonites. Meteoritics and Planetary Science, 46,
471 A77.
472 Giannini, M., Ballaran Tiziana, B., and Langenhorst, F. (2014) Crystal chemistry of synthetic
473 Ti–Mg-bearing hibonites: a single-crystal X-ray study. American Mineralogist, 99, 2060–
474 2067.
475 Göbbels, M., Woermann, E., and Jung, J. (1995) The Al-rich part of the system CaO-Al_2O_3-MgO.
476 I: Phase relationships. Journal of Solid State Chemistry, 120, 358–363.
477 Grossman, L. (1972) Condensation in the primitive solar nebula. Geochimica et Cosmochimica
478 Acta, 36, 597–619.
479 Grossman, L. (2010) Vapor-condensed phase processes in the early solar system. Meteoritics and
480 Planetary Science, 45, 7–20.
481 Grossman, L., Beckett, J.R., Fedkin, A.V., Simon, S.B., and Ciesla, F.J. (2008) Redox conditions
482 in the solar nebula: Observational, experimental, and theoretical constraints. In G.J.
483 MacPherson, D.W. Mittlefehldt, and J.H. Jones, Eds., Oxygen in the Solar System, 68,
484 93–140. Reviews in Mineralogy and Geochemistry, Mineralogical Society of America,
485 Chantilly, Virginia.
486 Han, J., and Brearley, A.J. (2017) Microstructures and formation history of melilite-rich
487 calcium–aluminum-rich inclusions from the ALHA77307 CO3.0 chondrite. Geochimica
488 et Cosmochimica Acta, 201, 136–154.

Always consult and cite the final, published document. See http:/www.minsocam.org or GeoscienceWorld

This is the peer-reviewed, final accepted version for American Mineralogist, published by the Mineralogical Society of America.
The published version is subject to change. Cite as Authors (Year) Title. American Mineralogist, in press.
DOI: https://doi.org/10.2138/am-2022-8014. http://www.minsocam.org/

Han, J., Brearley, A.J., and Keller, L.P. (2015) Microstructural evidence for a disequilibrium condensation origin for hibonite-spinel inclusions in the ALHA77307 CO3.0 chondrite. Meteoritics and Planetary Science, 50, 2121–2136.

Han, J., Liu, M.-C., Kööp, L., Keller, L.P., and Davis, A.M. (2017) Correlations among microstructure, morphology, chemistry, and isotopic systematics of hibonite in CM chondrites. 80th Annual Meeting of the Meteoritical Society, LPI contribution no.1987, abstract 6380.

Han, J., Jacobsen, B., Liu, M.-C., Brearley, A.J., Matzel, J.E., and Keller, L.P. (2019) Origin of ^{16}O-rich fine-grained Ca-Al-rich inclusions of different mineralogy and texture. Geochemistry, 79, 125543.

Han, J., Keller, L.P., Liu, M.-C., Needham, A.W., Hertwig, A.T., Messenger, S., and Simon, J.I. (2020) A coordinated microstructural and isotopic study of a Wark-Lovering rim on a Vigarano CAI. Geochimica et Cosmochimica Acta, 269, 639–660.

Hirotsu, Y., and Sato, H. (1978) Microsyntactic intergrowth and defects in barium ferrite compounds. Journal of Solid State Chemistry, 26, 1–16.

Hofmeister, A.M., Wopenka, B., and Locock, A.J. (2004) Spectroscopy and structure of hibonite, grossite, and $CaAl_2O_4$: Implications for astronomical environments. Geochimica et Cosmochimica Acta, 68, 4485–4503.

Ihinger, P.D., and Stolper, E. (1986) The color of meteoritic hibonite: An indicator of oxygen fugacity. Earth and Planetary Science Letters, 78, 67–79.

Ireland, T.R. (1988) Correlated morphological, chemical, and isotopic characteristics of hibonites from the Murchison carbonaceous chondrite. Geochimica et Cosmochimica Acta, 52, 2827–2839.

Always consult and cite the final, published document. See http:/www.minsocam.org or GeoscienceWorld

This is the peer-reviewed, final accepted version for American Mineralogist, published by the Mineralogical Society of America.
The published version is subject to change. Cite as Authors (Year) Title. American Mineralogist, in press.
DOI: https://doi.org/10.2138/am-2022-8014. http://www.minsocam.org/

512 Ireland, T.R. (1990) Presolar isotopic and chemical signatures in hibonite-bearing refractory
513 inclusions from the Murchison carbonaceous chondrite. Geochimica et Cosmochimica
514 Acta, 54, 3219–3237.
515 Iyi, N., Göbbels, M., and Matsui, Y. (1995) The Al-rich part of the system CaO-Al_2O_3-MgO. II:
516 Structure refinement of two new magnetoplumbite-related phases. Journal of Solid State
517 Chemistry, 120, 364–371.
518 Keller, L.P. (1991) Stacking disorder and non-stoichiometry in meteoritic hibonite. AGU Spring
519 Meeting Abstract M21A-02, EOS, Transactions, American Geophysical Union 72, 141.
520 Kööp, L., Nakashima, D., Heck, P.R., Kita, N.T., Tenner, T.J., Krot, A.N., Nagashima, K., Park,
521 C., and Davis, A.M. (2016) New constraints on the relationship between ^{26}Al and oxygen,
522 calcium, and titanium isotopic variation in the early Solar System from a multielement
523 isotopic study of spinel-hibonite inclusions. Geochimica et Cosmochimica Acta, 184,
524 151–172.
525 Kööp, L., Davis, A.M., Krot, A.N., Nagashima, K., and Simon, S.B. (2018) Calcium and
526 titanium isotopes in refractory inclusions from CM, CO, and CR chondrites. Earth and
527 Planetary Science Letters, 489, 179–190.
528 Krot, A.N., Ma, C., Nagashima, N., Davis, A.M., Beckett, J.R., Simon, S.B., Komatsu, M.,
529 Fagan, T.J., Brenker, F., Ivanona, M.A., and Bischoff, A. (2019) Mineralogy,
530 petrography, and oxygen isotopic compositions of ultrarefractory inclusions from
531 carbonaceous chondrites. Geochemistry, 79, 125519.
532 Liu, M.-C., and McKeegan, K.D. (2009) On an irradiation origin for magnesium isotope
533 anomalies in meteoritic hibonite. The Astrophysical Journal, 697, L145–L148.
534 Liu, M.-C., Han, J., Brearley, A.J., and Hertwig, A.T. (2019) Aluminum-26 chronology of dust

Always consult and cite the final, published document. See http:/www.minsocam.org or GeoscienceWorld

This is the peer-reviewed, final accepted version for American Mineralogist, published by the Mineralogical Society of America.
The published version is subject to change. Cite as Authors (Year) Title. American Mineralogist, in press.
DOI: https://doi.org/10.2138/am-2022-8014. http://www.minsocam.org/

coagulation and early solar system evolution. Science Advances, 5, eaaw3350.

Ma, C., Krot, A.N., Beckett, J.R., Nagashima, K., Tschauner, O., Rossman, G.R., Simon, S.B., and Bischoff, A. (2020) Warkite, $Ca_2Sc_6Al_6O_{20}$, a new mineral in carbonaceous chondrites and a key-stone phase in ultrarefractory inclusions from the solar nebula. Geochimica et Cosmochimica Acta, 277, 52–86.

MacPherson, G.J. (2014) Calcium-aluminum-rich inclusions in chondritic meteorites. In K. Turekian and H. Holland, Eds., Treatise on Geochemistry 2nd edition, p. 139–179. Oxford, Elsevier-Pergamon.

MacPherson, G., Grossman, L., Hashimoto, A., Bar-Matthews, M., and Tanaka, T. (1984) Petrographic studies of refractory inclusions from the Murchison meteorite. Proceeding of the 15th lunar and planetary science conference, Journal of Geophysical Research Supplement, 89, C299–C312.

Nagashima, M., Armbruster, T., and Hainschwang, T. (2010) A temperature-dependent structure study of gem-quality hibonite from Myanmar. Mineralogical Magazine, 74, 871–885.

Navrotsky, A., Wechsler, B.A., Geisinger, K., and Seifert, F. (1986) Thermochemistry of $MgAl_2O_4$–$Al_{8/3}O_4$ defect spinels. Journal of the American Ceramic Society, 69, 418–422.

Needham, A.W., Messenger, S., Han, J., and Keller, L.P. (2017) Corundum–hibonite inclusions and the environments of high temperature processing in the early Solar System. Geochimica et Cosmochimica Acta, 196, 18–35.

Ohnishi, I., Suzuki, T., Miyatake, K., Jimbo, Y., Iwasawa, Y., Morita, M., Sasaki, T., Sawada, H., and Okunishi, E. (2018) Analytical and in situ applications using aberration corrected scanning transmission electron microscope. e-Journal of Surface Science and Nanotechnology, 16, 286–288.

Always consult and cite the final, published document. See http:/www.minsocam.org or GeoscienceWorld

Sack, R. O. (2014) $MgAl_2O_4$-$Al_{8/3}O_4$ spinels: Formulation and calibration of the low-pressure thermodynamics of mixing. American Journal of Science, 314, 858–877.

Sahijpal, S., Goswami, J.N., and Davis, A.M. (2000) K, Mg, Ti and Ca isotopic compositions and refractory trace element abundances in hibonites from CM and CV meteorites: Implications for early solar system processes. Geochimica et Cosmochimica Acta, 64, 1989–2005.

Schmid, H., and De Jonghe, L.C. (1983) Structure and nonstoichiometry of calcium aluminates. Philosophical Magazine A, 48, 287–297.

Simon, S.B., Yoneda, S., Grossman, L., and Davis, A.M. (1994) A $CaAl_4O_7$-bearing refractory spherule from Murchison: Evidence for very high-temperature melting in the solar nebula. Geochimica et Cosmochimica Acta, 58, 1937–1949.

Simon, S.B., Grossman, L., and Davis, A.M. (1997) Multiple generations of hibonite in spinel-hibonite inclusions from Murchison. Meteoritics and Planetary Science, 32, 259–269.

Simon, S.B., Davis, A.M., and Grossman, L. (2001) Formation of orange hibonite, as inferred from some Allende inclusions. Meteoritics and Planetary Science, 36, 331–350.

Simon, S.B., Grossman, L., Hutcheon, I.D., Phinney, D.L., Weber, P.K., and Fallon, S.J. (2006) Formation of spinel-, hibonite-rich inclusions found in CM2 carbonaceous chondrites. American Mineralogist, 91, 1675–1687.

Stoyanov, E., Langenhorst, F., and Steinle-Neumann, G. (2007) The effect of valence state and site geometry on Ti $L_{3,2}$ and O K electron energy-loss spectra of Ti_xO_y phases. American Mineralogist, 92, 577–586.

Thompson, J.B. (1978) Biopyriboles and polysomatic series. American Mineralogist, 63, 239–249.

Always consult and cite the final, published document. See http:/www.minsocam.org or GeoscienceWorld

This is the peer-reviewed, final accepted version for American Mineralogist, published by the Mineralogical Society of America.
The published version is subject to change. Cite as Authors (Year) Title. American Mineralogist, in press.
DOI: https://doi.org/10.2138/am-2022-8014. http://www.minsocam.org/

581 Toppani, A., Libourel, G., Robert, F., and Ghanbaja, J. (2006) Laboratory condensation of
582 refractory dust in protosolar and circumstellar conditions. Geochimica et Cosmochimica
583 Acta, 70, 5035–5060.
584 Veblen, D.R. (1991) Polysomatism and polysomatic series: A review and applications. American
585 mineralogist, 76,801–826.
586 Zega, T.J., Nittler, L.R., Stroud, R.M., Alexander, C.M.O'D., and Kilcoyne, A.L.D. (2012)
587 Measurement of the oxidation state of Ti in solar and presolar hibonite. Proceedings of
588 the 43rd Lunar and Planetary Science Conference, Lunar and Planetary Institute, Houston,
589 TX, abstract 2338.
590 Zega, T.J., Manga, V., Domanik, K., and Muralidiharan, K. (2016) Nanostructural analysis of
591 several perovskite grains from an Allende CAI: Evidence for equilibrium or non-
592 equilibrium condensation? Proceedings of the 47th Lunar and Planetary Science
593 Conference, Lunar and Planetary Institute, Houston, TX, abstract 2807.

Always consult and cite the final, published document. See http:/www.minsocam.org or GeoscienceWorld

This is the peer-reviewed, final accepted version for American Mineralogist, published by the Mineralogical Society of America.
The published version is subject to change. Cite as Authors (Year) Title. American Mineralogist, in press.
DOI: https://doi.org/10.2138/am-2022-8014. http://www.minsocam.org/

FIGURE CAPTIONS

Figure 1. SEM images of CAI *LK44* from Allende. (a) Combined elemental map in Mg (red), Ca (green), and Al (blue) of the entire view of the CAI from the thin section. The outlined region in (a) is shown in detail in (b, c). (b, c) Enlarged BSE image and corresponding false color elemental X-ray map inMg (red), Ti (green), and Al (blue) of a hibonite-spinel inclusion in melilite. Perovskite also occurs attached to hibonite. Note the oscillatory Ti and Mg zoning in hibonite grains. In (b), the FIB section locations are indicated by dashed lines. Abbreviations hereafter: hib = hibonite; pv = perovskite; sp = spinel; mel = melilite; WL rim = Wark-Lovering rim.

Figure 2. SEM BSE images of the reaction zones from experiments (2-4) showing a similar mineral sequence from hibonite, grossite, to krotite + quenched melt glass. Elongated spinel, indicated by arrows, occurs intergrown with hibonite only from experiment (2) in (a), whereas euhedral spinel are present in grossite and krotite + glass from all experiments in (b, c). Abbreviations hereafter: cor = corundum; grs = grossite; krt = krotite.

Figure 3. TEM images of two FIB sections from hibonite in the CAI *LK44*. (a, d) BF STEM images and (b, e) corresponding elemental X-ray maps in Mg (red), Ti (green), and Al (blue) of the entire FIB-A and -B sections. The oscillatory Ti and Mg zoning in hibonite grains is apparent. The outlined area in (a, d) is shown in detail in (c, f). (c, f) Enlarged BF STEM images of hibonite crystals HIB-1 and HIB-2, which contain planar defects normal to the *c* axis. Inset diffraction patterns are indexed as the [100] zone axis of hibonite.

Always consult and cite the final, published document. See http:/www.minsocam.org or GeoscienceWorld

This is the peer-reviewed, final accepted version for American Mineralogist, published by the Mineralogical Society of America.
The published version is subject to change. Cite as Authors (Year) Title. American Mineralogist, in press.
DOI: https://doi.org/10.2138/am-2022-8014. http://www.minsocam.org/

Figure 4. TEM images of an Al-rich spinel inclusion in hibonite from the CAI *LK44*. (a) BF STEM image of the spinel inclusion decorated by step-wise defects, indicated by arrows. Inset diffraction patterns are indexed as the [100] zone axis of the host hibonite crystal HIB-3. (b) HRTEM image of the spinel inclusion that is in a crystallographic continuity with the host hibonite HIB-3. (c, d) FFT patterns of the spinel inclusion and the host hibonite HIB-3 obtained from HRTEM images shown in (c). A crystallographic orientation relationship exists between the host hibonite and the spinel inclusion, such that $[100]_{hibonite}//[011]_{spinel}$ and $(001)_{hibonite}//(111)_{spinel}$.

Figure 5. BF STEM images of synthetic hibonite crystals from experiments (2-4). Mg-bearing hibonite (a, b) contains a higher density of defects than Mg-Ti-bearing hibonite (c), irrespective of the heating duration.

Figure 6. Correlation between defects and chemical compositions of synthetic hibonite. (a) BF STEM image and (b) corresponding Mg X-ray map of defect-bearing area in the Mg-bearing hibonite crystal from experiment (2). The vertical dark bands in (a), indicated by arrows and bracket, represent defects in the hibonite crystal. (c) Profile of Mg concentrations extracted from the spectrum map shown in (b).

Figure 7. HAADF images of hibonite crystals from the CAI *LK44*. (a, b) A hibonite crystal HIB-1 from FIB-A. Isolated layers of 1.6 nm (002) spacing are randomly intergrown with prominent layers of 1.1 nm (002) spacing. (c, d) A hibonite crystal HIB-2 from FIB-B. A rare layer of 2.5 nm (002) spacing, as well as an isolated layer of 1.6 nm (002) spacing, are observed within

Always consult and cite the final, published document. See http:/www.minsocam.org or GeoscienceWorld

prominent layers of 1.1 nm (002) spacing. The brightest white and grey spots arise from Ca and Al atoms, respectively, whereas Ti and Mg atoms are not readily visible in these images. All images were taken along the $[1\bar{1}0]$ zone axis of hibonite, as shown in inset FFT patterns in (b).

Figure 8. HAADF images of an Al-rich spinel inclusion in hibonite from the CAI *LK44*. The spinel inclusion is decorated by a single layer of 1.6 nm (002) spacing along its top (a), as well as stepwise layers of 2.0 nm (002) spacing extended from its bottom end (b-d). The brightest white and grey spots arise from Ca and Al atoms, respectively, whereas Ti and Mg atoms are not readily visible in these images. All images were taken along the $[1\bar{1}0]$ zone axis of hibonite, as shown in inset FFT patterns in (c).

Figure 9. Projected structures of hibonite in terms of structural unit S and R blocks. The CrystalMaker^{TM} software was used to draw the hibonite structure model in the $[1\bar{1}0]$ zone axis, adopted from single-crystal X-ray diffraction data (Nagashima et al. 2010). Bottom insets show the distribution of five Al sites (M1-M5) and preferential Ti and Mg substitution. While Al is distributed over five sites, Mg occupies only M3 sites in S blocks and Ti partitions between M2 and M4 sites in R blocks.

Figure 10. Atomic-scale elemental X-ray maps and profiles of Ca, Al, Mg, and Ti obtained from hibonite crystals from the CAI *LK44*. The reference HAADF images and corresponding X-ray maps were taken along the $[1\bar{1}0]$ zone axis of hibonite.

Figure 11. Cations per formula unit in hibonite from the CAI *LK44*. The chemical compositions

Always consult and cite the final, published document. See http:/www.minsocam.org or GeoscienceWorld

This is the peer-reviewed, final accepted version for American Mineralogist, published by the Mineralogical Society of America.
The published version is subject to change. Cite as Authors (Year) Title. American Mineralogist, in press.
DOI: https://doi.org/10.2138/am-2022-8014. http://www.minsocam.org/

663 of hibonite grains from FIB-B were extracted from spectrum maps shown in Figure 3b, obtained
664 using TEM EDX. All Ti was calculated as Ti^{4+}.

665

666 **Figure 12.** (a) EELS data for the Ti $L_{2,3}$ edge in hibonite and perovskite in FIB-A from the
667 CAI *LK44*. The hibonite spectrum shows well-resolved Ti^{3+} shoulders on the L_3 edge (labeled "A"
668 and "B") that occur at 458.1 eV and 460.4 eV, respectively. (b) Gaussian peak fits for the
669 Ti^{3+} and Ti^{4+} components in the hibonite Ti L_3 edge**.** Hibonite contains ~15-20% of Ti as Ti^{3+}, in
670 contrast to perovskite containing Ti^{4+} only.

Always consult and cite the final, published document. See http:/www.minsocam.org or GeoscienceWorld

This is the peer-reviewed, final accepted version for American Mineralogist, published by the Mineralogical Society of America.
The published version is subject to change. Cite as Authors (Year) Title. American Mineralogist, in press.
DOI: https://doi.org/10.2138/am-2022-8014. http://www.minsocam.org/

671 **TABLES**

672 **Table 1.** Representative electron microprobe data of hibonite and spinel in the Allende CAI

673 *LK44*.

Mineral	Hibonite		Hibonite		Spinel		Spinel	
Analysis #	1		2		3		4	
	wt%	SD	wt%	SD	wt%	SD	wt%	SD
SiO_2	0.16	0.02	0.09	0.02	bd	-	bd	-
TiO_2	7.54	0.14	6.69	0.14	0.12	0.04	0.11	0.04
Al_2O_3	78.80	0.46	79.76	0.47	69.44	0.42	69.30	0.42
Cr_2O_3	0.06	0.04	0.05	0.04	0.08	0.04	0.12	0.04
V_2O_3	0.47	0.09	0.60	0.09	0.84	0.10	0.91	0.11
FeO	0.12	0.08	bd	-	0.51	0.11	1.08	0.15
MgO	3.72	0.08	3.38	0.07	27.57	0.33	27.24	0.33
CaO	8.18	0.17	8.37	0.17	0.12	0.03	0.15	0.03
Total	99.05		98.94		98.68		98.91	
Cation								
Si	0.018		0.010		-		-	
Ti	0.649		0.575		0.002		0.002	
Al	10.632		10.755		1.975		1.972	
Cr	0.005		0.004		0.001		0.002	
V	0.043		0.055		0.016		0.018	
Fe	0.012		-		0.010		0.022	
Mg	0.634		0.576		0.992		0.981	
Ca	1.003		1.026		0.003		0.004	
Sum	12.996		13.001		2.999		3.001	

674 Note: Cation formula were calculated based on 19 and 4 oxygen anions for hibonite and spinel,

675 respectively. SD = Standard deviation. bd = below detection.

Always consult and cite the final, published document. See http:/www.minsocam.org or GeoscienceWorld

This is the peer-reviewed, final accepted version for American Mineralogist, published by the Mineralogical Society of America.
The published version is subject to change. Cite as Authors (Year) Title. American Mineralogist, in press.
DOI: https://doi.org/10.2138/am-2022-8014. http://www.minsocam.org/

676 **Table 2.** A summary of experimental conditions and products for synthetic hibonite samples.

#	Starting melt composition	Heating duration	Phases observed	Planar defects in hibonite	Hibonite composition (wt%)	
					MgO	TiO_2
1	2CaO-Al_2O_3 eutectic	4 hours	hib, gro, kr+gls	−	-	-
2	+ 5 wt% MgO	4 hours	hib+sp, gro, kr+sp+gls	+++	0.2	-
3	+ 5 wt% MgO	5 days	hib, gro+sp, kr+gls	+++	0.2	-
4	+ 5 wt% MgO + $CaTiO_3$	5 days	hib, gro+sp, kr+sp+gls	+	<1	<0.5
5	+ $CaTiO_3$	5 days	hib, gro, pv+gls	−	-	1

677 Note: The chemical compositions were determined by TEM EDX. Abbreviations: hib = hibonite, sp = spinel, gro = grossite, kr =

678 krotite, gls = quenched glass.

Always consult and cite the final, published document. See http:/www.minsocam.org or GeoscienceWorld

This is the peer-reviewed, final accepted version for American Mineralogist, published by the Mineralogical Society of America.
The published version is subject to change. Cite as Authors (Year) Title. American Mineralogist, in press.
DOI: https://doi.org/10.2138/am-2022-8014. http://www.minsocam.org/

Figure 1

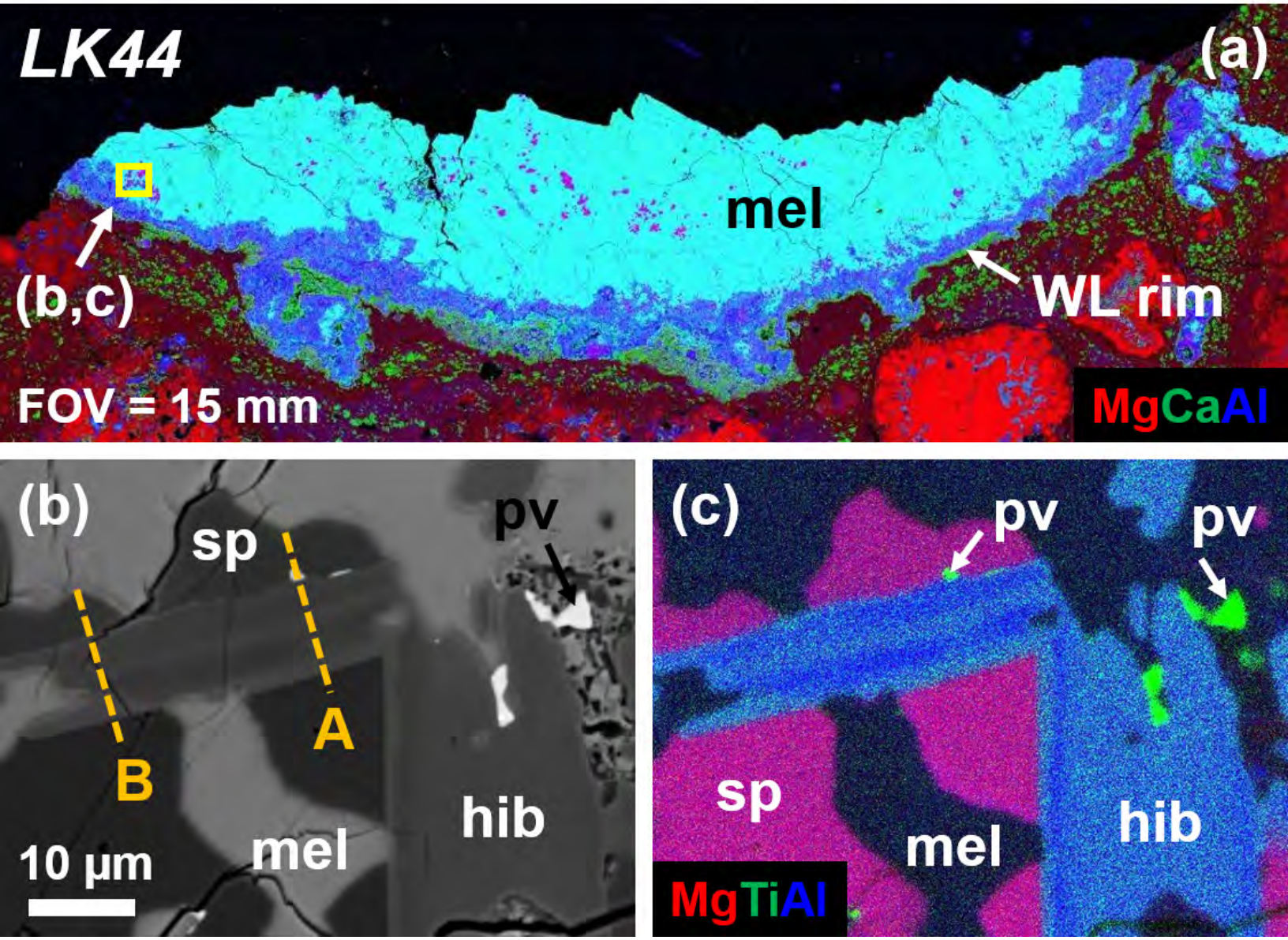

Always consult and cite the final, published document. See http:/www.minsocam.org or GeoscienceWorld

This is the peer-reviewed, final accepted version for American Mineralogist, published by the Mineralogical Society of America.
The published version is subject to change. Cite as Authors (Year) Title. American Mineralogist, in press.
DOI: https://doi.org/10.2138/am-2022-8014. http://www.minsocam.org/

Figure 2

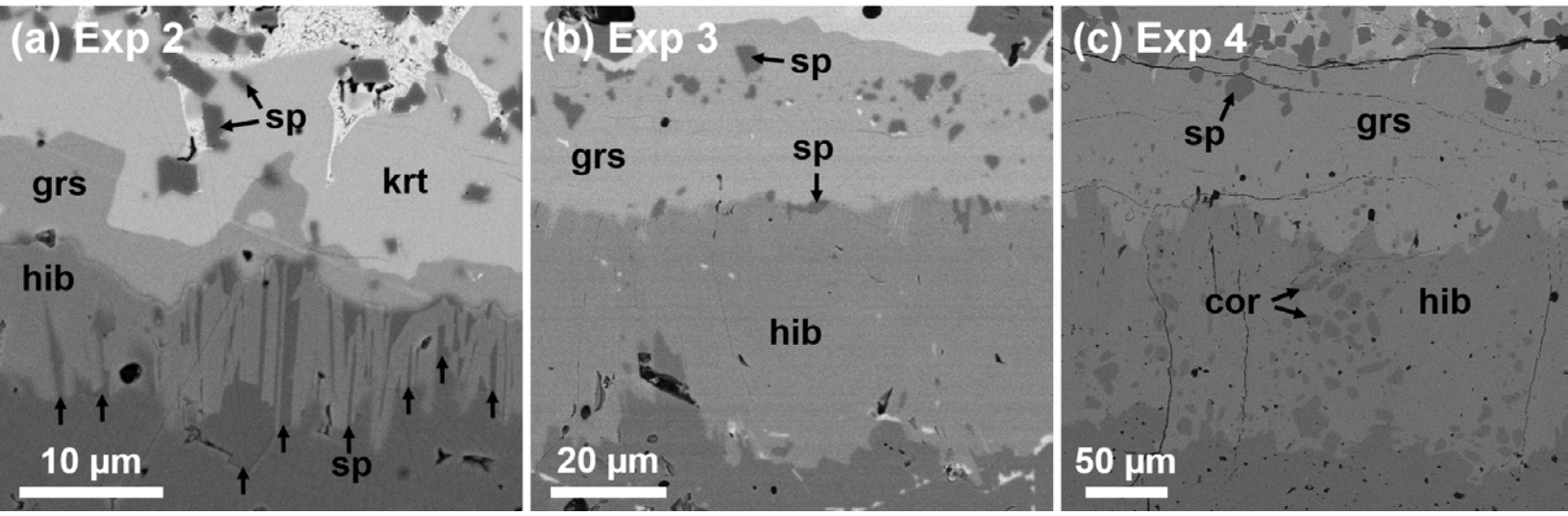

Always consult and cite the final, published document. See http:/www.minsocam.org or GeoscienceWorld

This is the peer-reviewed, final accepted version for American Mineralogist, published by the Mineralogical Society of America.
The published version is subject to change. Cite as Authors (Year) Title. American Mineralogist, in press.
DOI: https://doi.org/10.2138/am-2022-8014. http://www.minsocam.org/

Figure 3

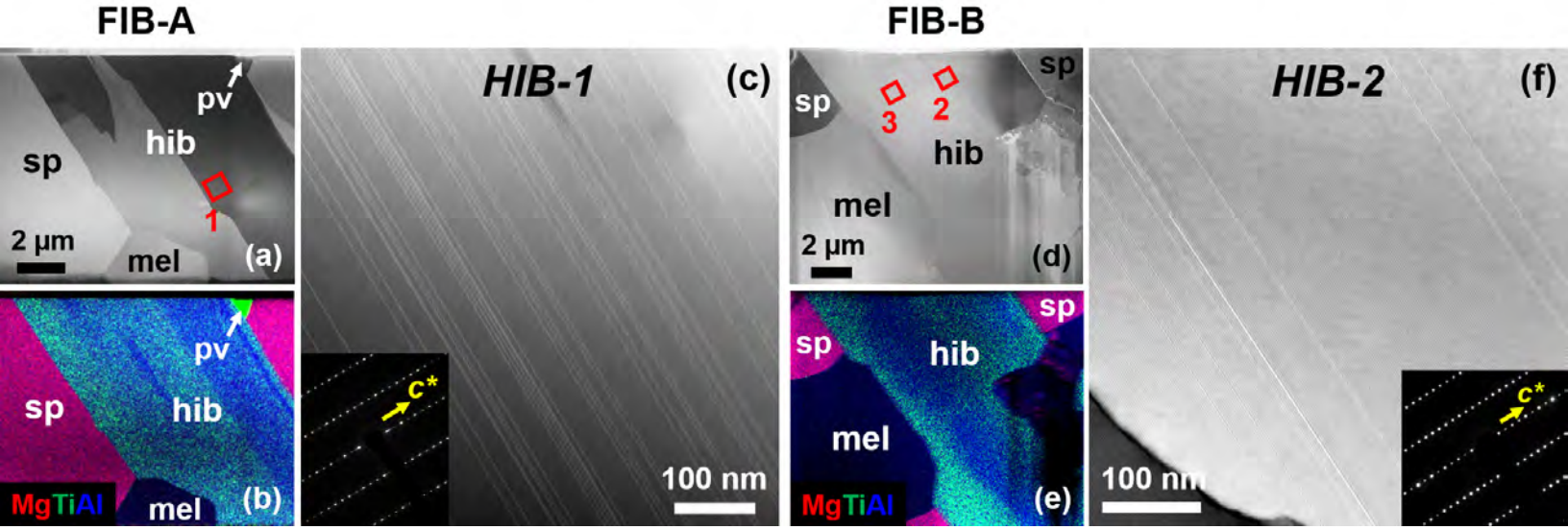

Always consult and cite the final, published document. See http:/www.minsocam.org or GeoscienceWorld

This is the peer-reviewed, final accepted version for American Mineralogist, published by the Mineralogical Society of America.
The published version is subject to change. Cite as Authors (Year) Title. American Mineralogist, in press.
DOI: https://doi.org/10.2138/am-2022-8014. http://www.minsocam.org/

Figure 4

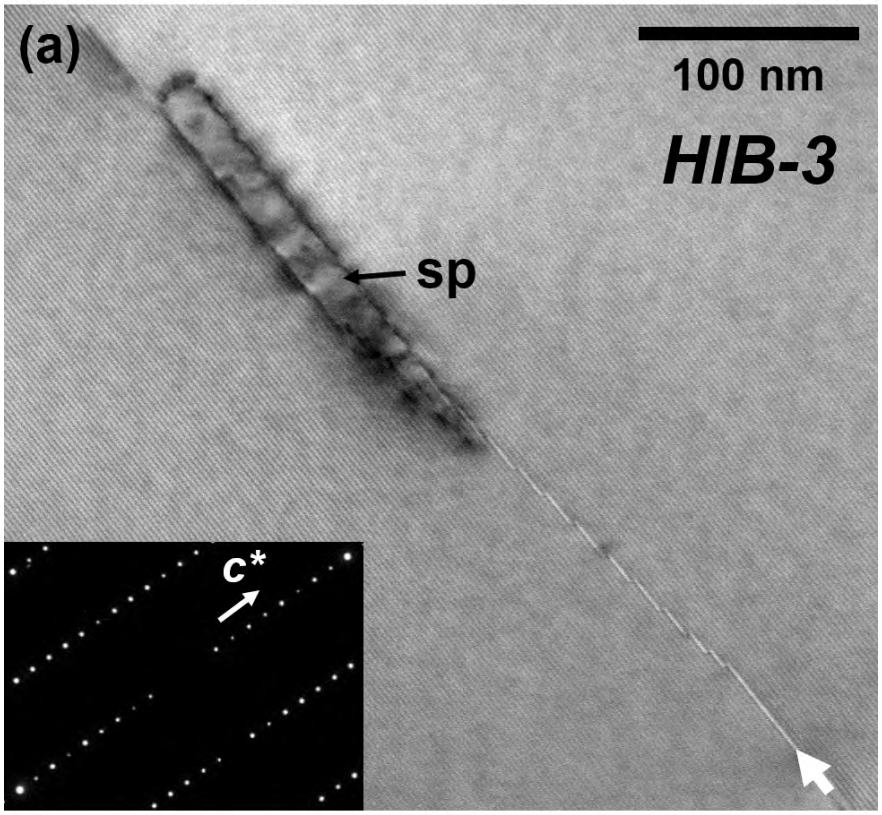

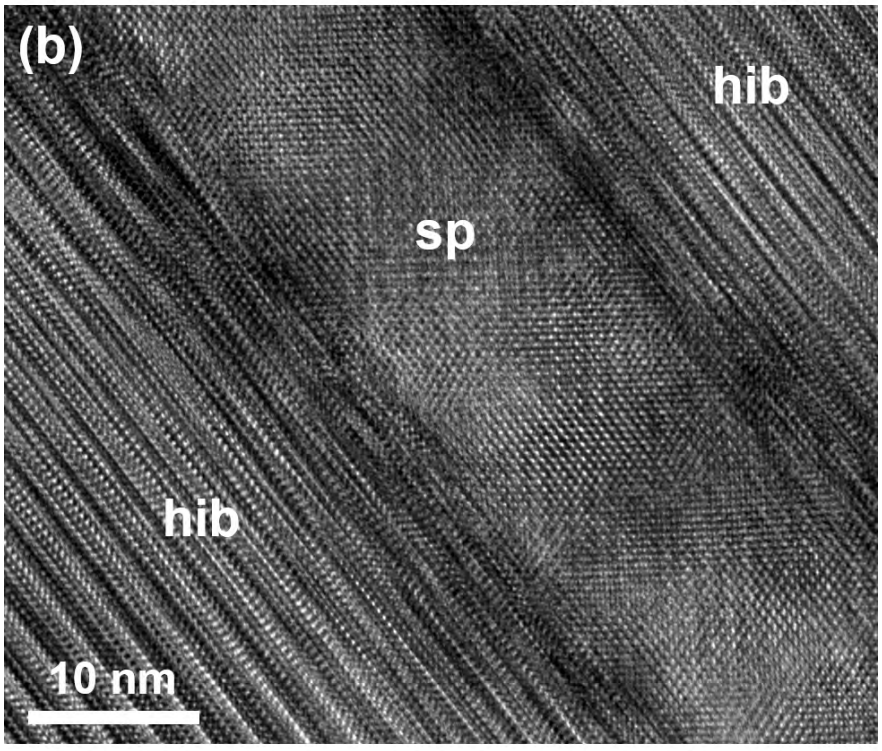

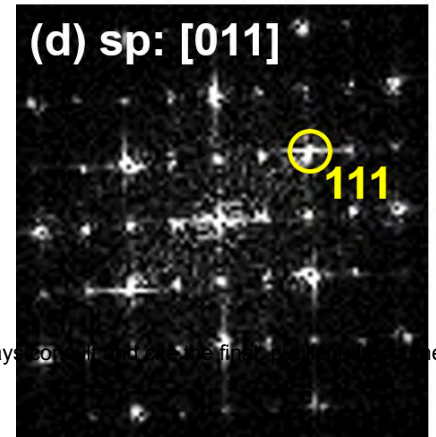

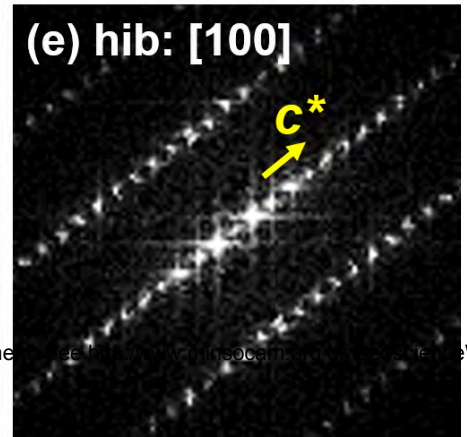

Always consult and cite the final, published document. See http://www.minsocam.org/MSA/AmMin/TOC/Journal_Publication_Info.html
World

This is the peer-reviewed, final accepted version for American Mineralogist, published by the Mineralogical Society of America.
The published version is subject to change. Cite as Authors (Year) Title. American Mineralogist, in press.
DOI: https://doi.org/10.2138/am-2022-8014. http://www.minsocam.org/

Figure 5

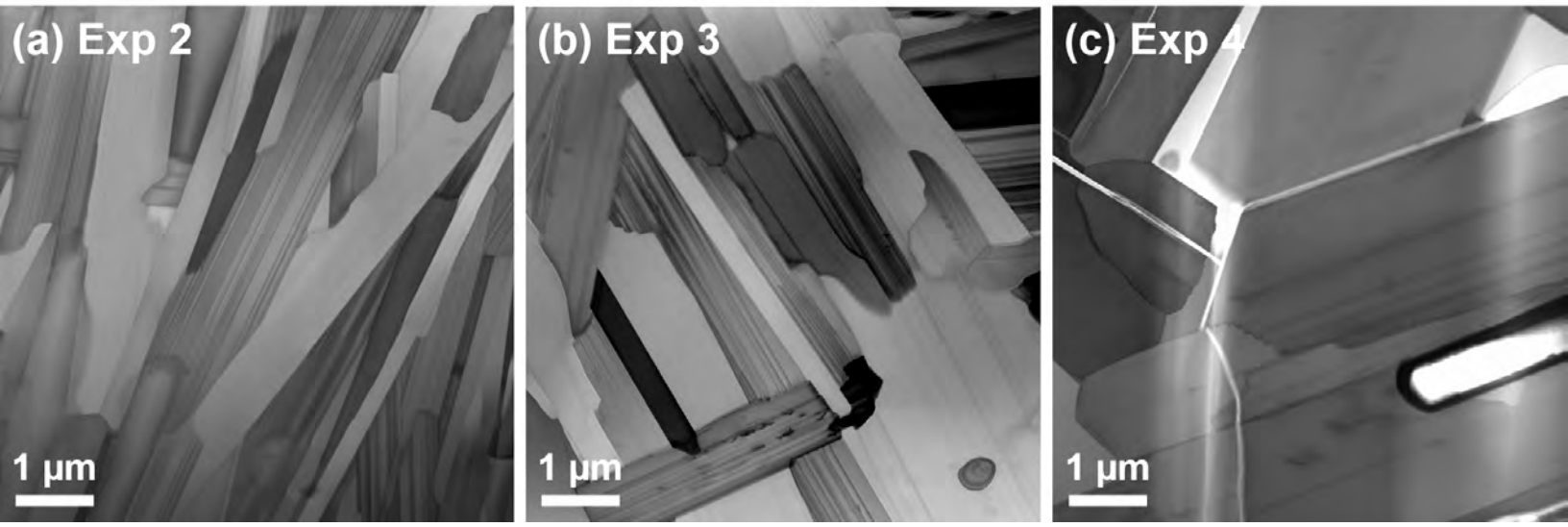

Always consult and cite the final, published document. See http:/www.minsocam.org or GeoscienceWorld

This is the peer-reviewed, final accepted version for American Mineralogist, published by the Mineralogical Society of America.
The published version is subject to change. Cite as Authors (Year) Title. American Mineralogist, in press.
DOI: https://doi.org/10.2138/am-2022-8014. http://www.minsocam.org/

Figure 6

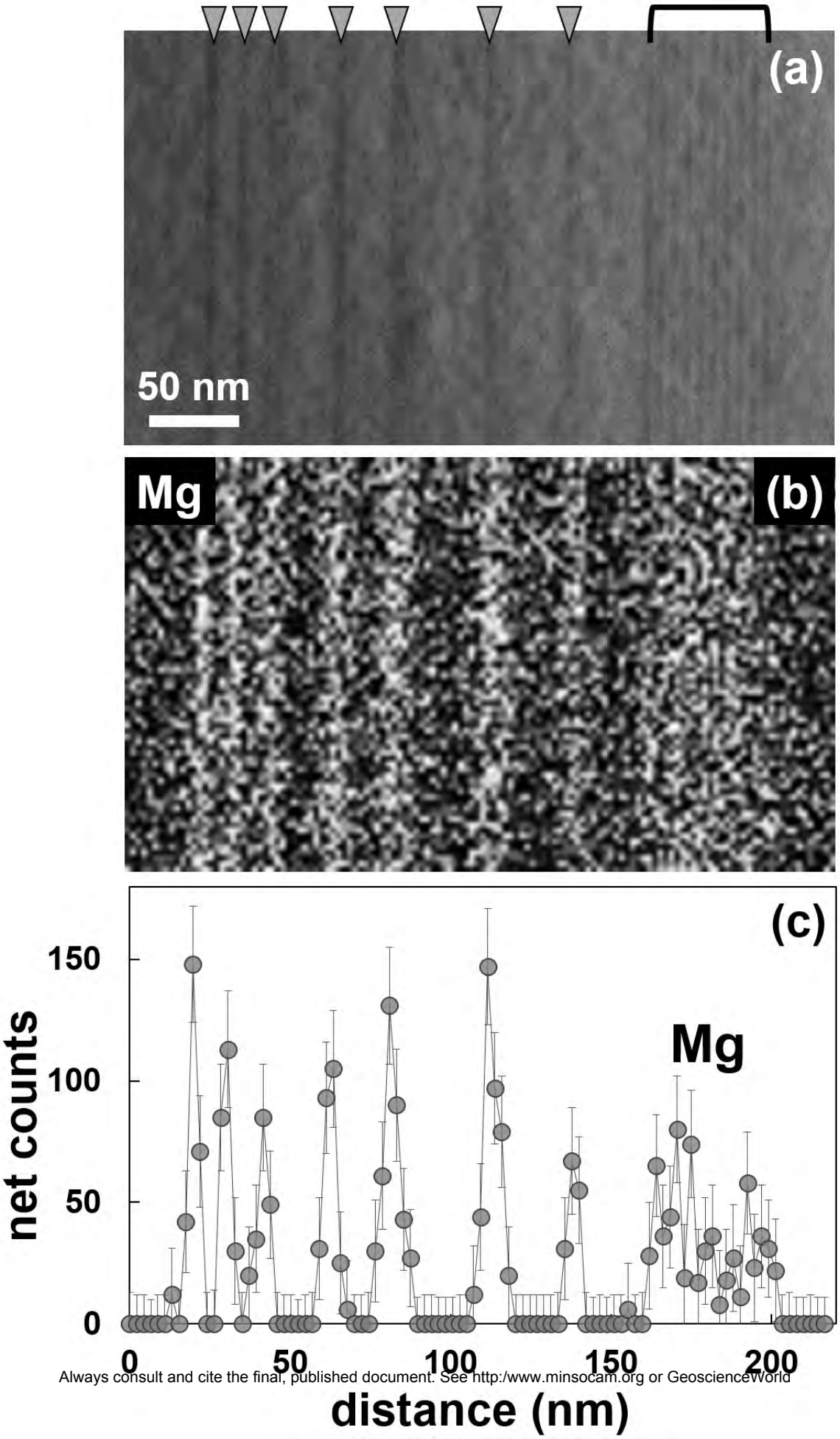

Always consult and cite the final, published document. See http:/www.minsocam.org or GeoscienceWorld

This is the peer-reviewed, final accepted version for American Mineralogist, published by the Mineralogical Society of America.
The published version is subject to change. Cite as Authors (Year) Title. American Mineralogist, in press.
DOI: https://doi.org/10.2138/am-2022-8014. http://www.minsocam.org/

Figure 7

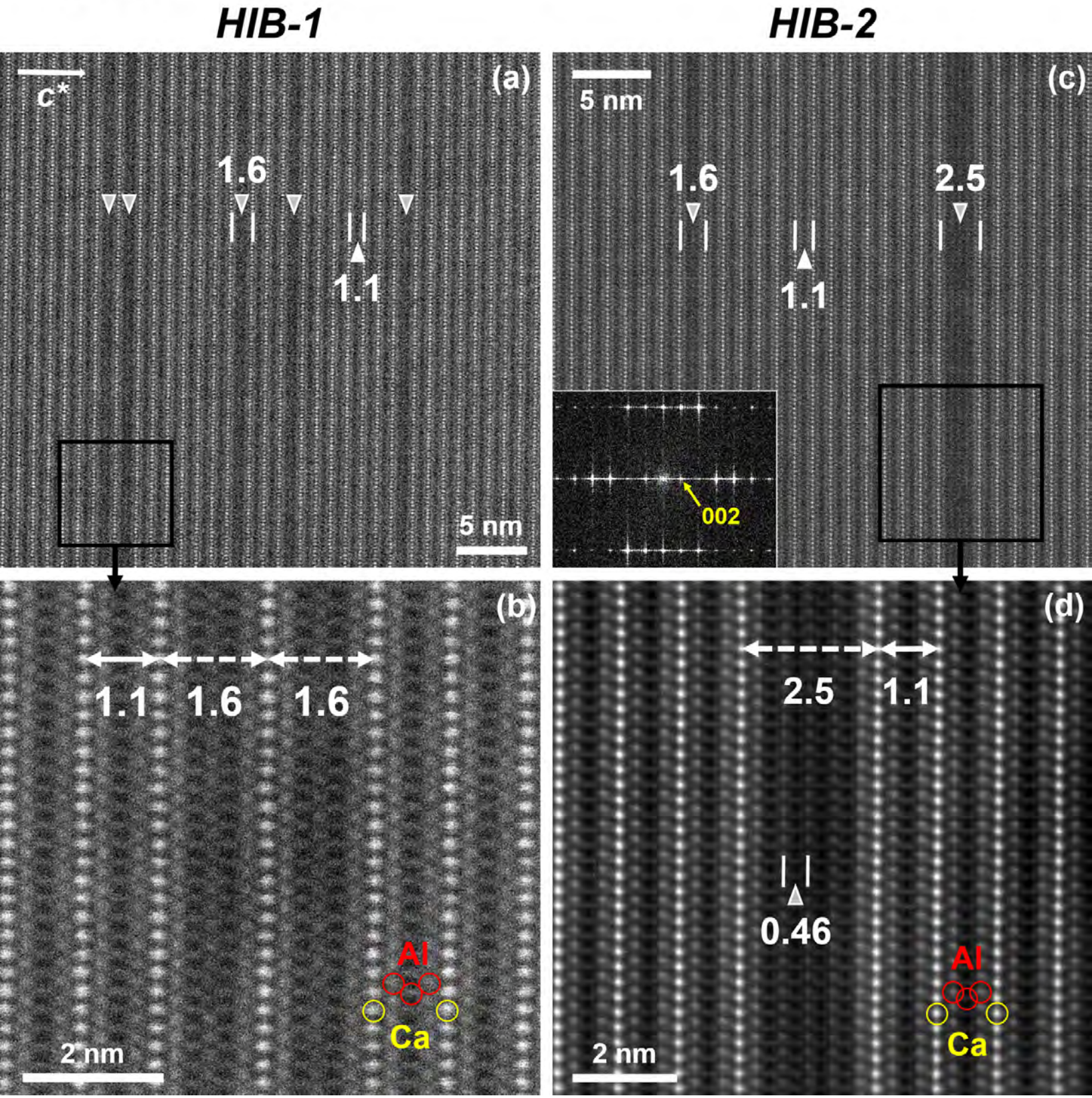

Always consult and cite the final, published document. See http:/www.minsocam.org or GeoscienceWorld

This is the peer-reviewed, final accepted version for American Mineralogist, published by the Mineralogical Society of America.
The published version is subject to change. Cite as Authors (Year) Title. American Mineralogist, in press.
DOI: https://doi.org/10.2138/am-2022-8014. http://www.minsocam.org/

Figure 8

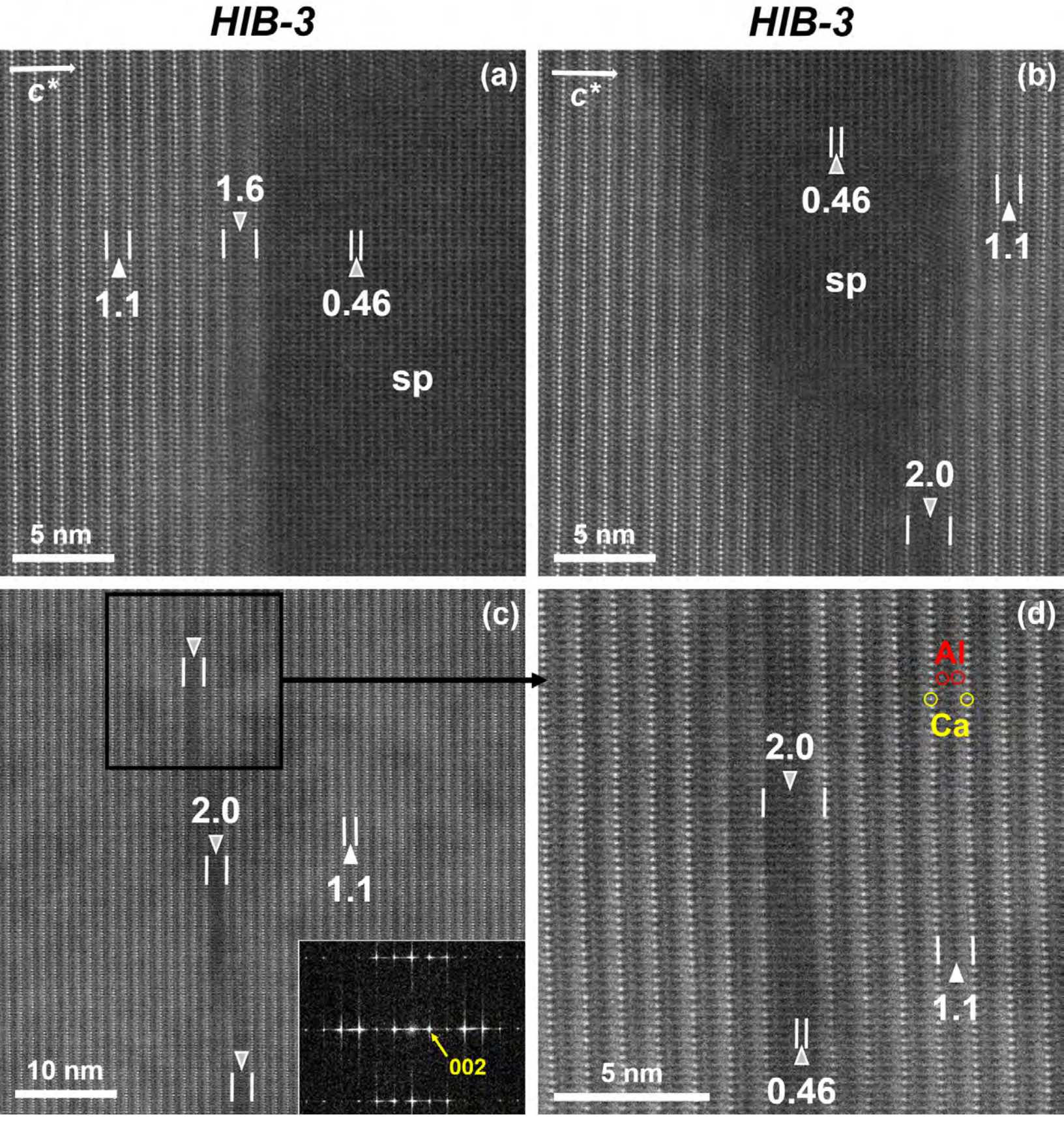

Always consult and cite the final, published document. See http:/www.minsocam.org or GeoscienceWorld

This is the peer-reviewed, final accepted version for American Mineralogist, published by the Mineralogical Society of America.
The published version is subject to change. Cite as Authors (Year) Title. American Mineralogist, in press.
DOI: https://doi.org/10.2138/am-2022-8014. http://www.minsocam.org/

Figure 9

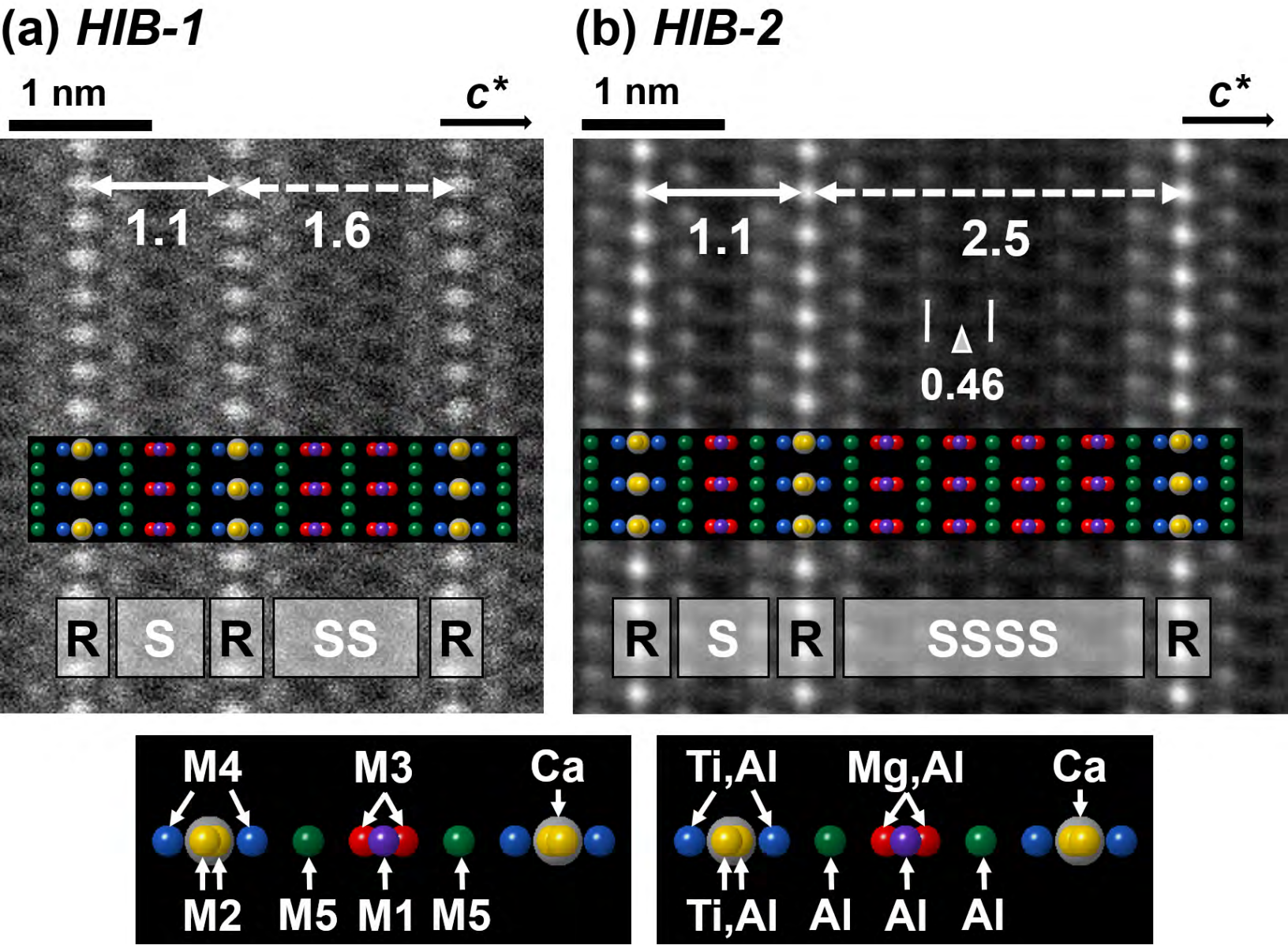

Always consult and cite the final, published document. See http:/www.minsocam.org or GeoscienceWorld

This is the peer-reviewed, final accepted version for American Mineralogist, published by the Mineralogical Society of America.
The published version is subject to change. Cite as Authors (Year) Title. American Mineralogist, in press.
DOI: https://doi.org/10.2138/am-2022-8014. http://www.minsocam.org/

Figure 10

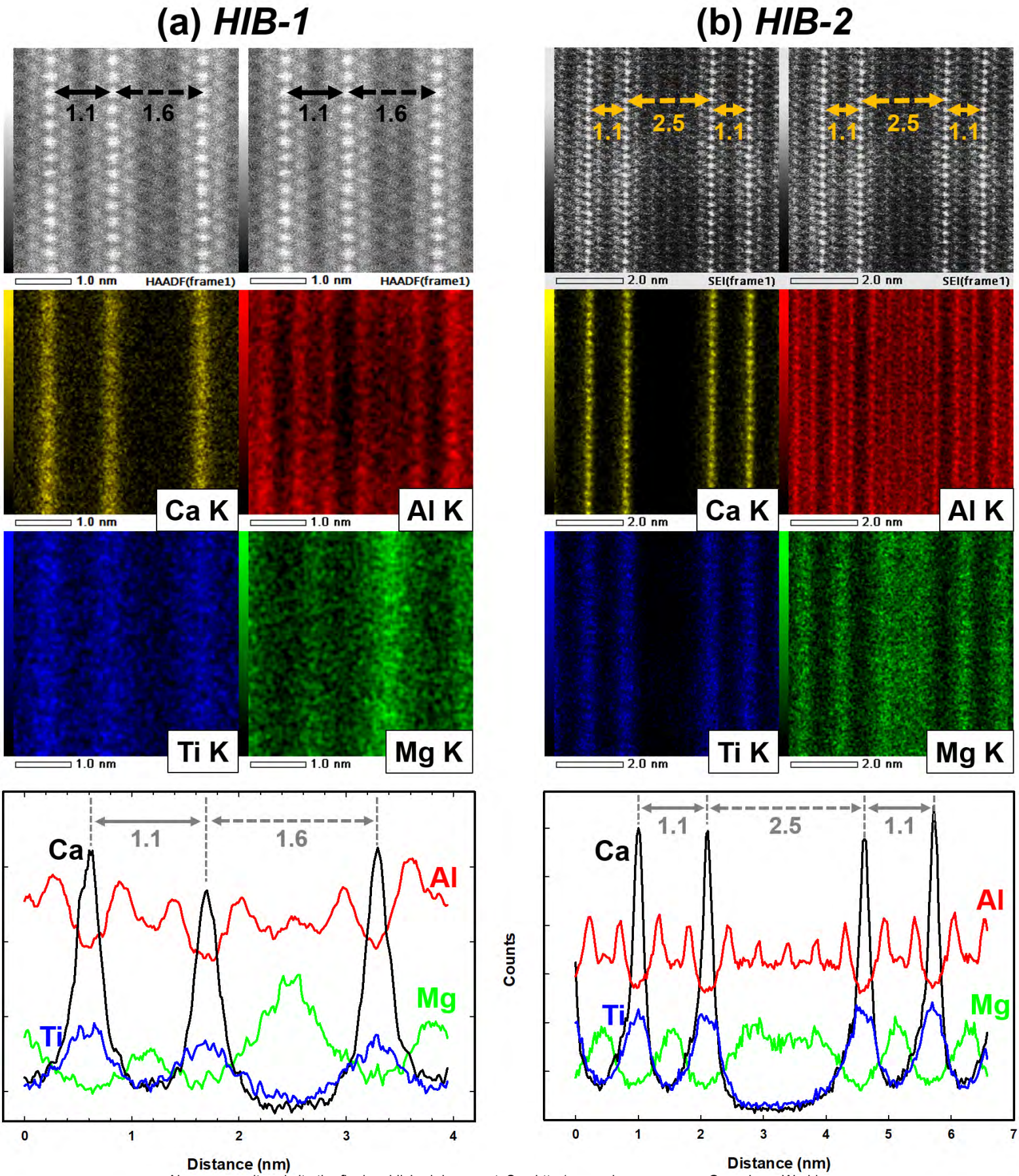

Always consult and cite the final, published document. See http:/www.minsocam.org or GeoscienceWorld

This is the peer-reviewed, final accepted version for American Mineralogist, published by the Mineralogical Society of America.
The published version is subject to change. Cite as Authors (Year) Title. American Mineralogist, in press.
DOI: https://doi.org/10.2138/am-2022-8014. http://www.minsocam.org/

Figure 11

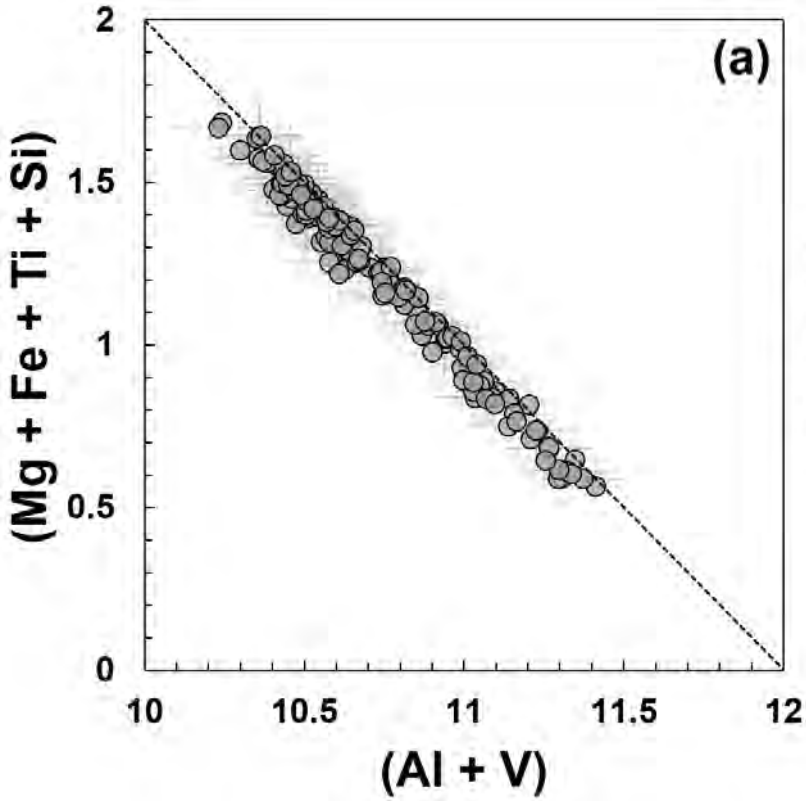

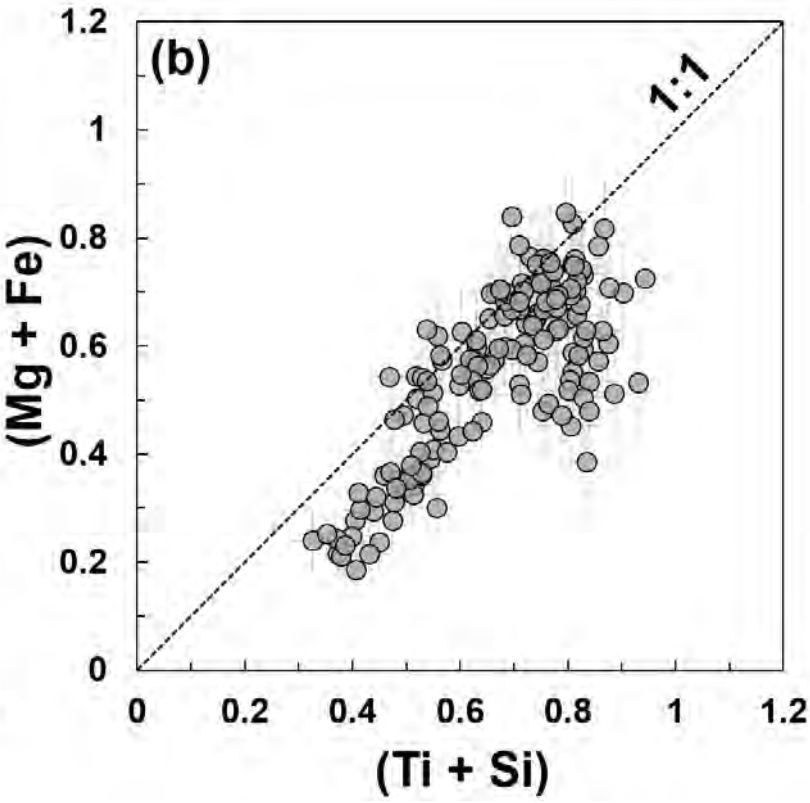

Always consult and cite the final, published document. See http:/www.minsocam.org or GeoscienceWorld

This is the peer-reviewed, final accepted version for American Mineralogist, published by the Mineralogical Society of America.
The published version is subject to change. Cite as Authors (Year) Title. American Mineralogist, in press.
DOI: https://doi.org/10.2138/am-2022-8014. http://www.minsocam.org/

Figure 12

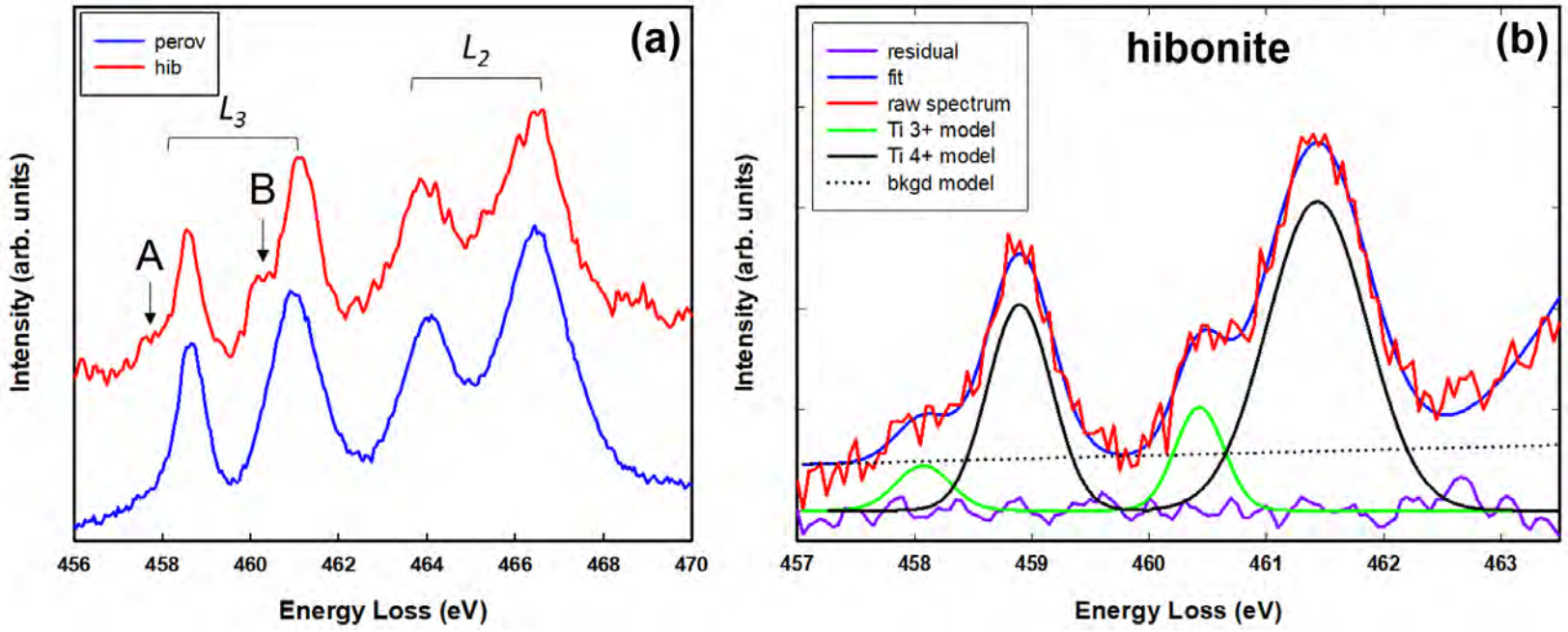

Always consult and cite the final, published document. See http:/www.minsocam.org or GeoscienceWorld